




# Metabolic plasticity sustains the robustness of *Caenorhabditis elegans* embryogenesis

Siyu Chen<sup>1,2</sup>, Xing Su<sup>1,2</sup>, Jinglin Zhu<sup>1,2</sup> , Long Xiao<sup>1,2</sup>, Yulin Cong<sup>1,2</sup>, Leilei Yang<sup>1,2</sup>, Zhuo Du<sup>1,2</sup>  & Xun Huang<sup>1,2,3,\*</sup> 

## Abstract

Embryogenesis is highly dependent on maternally loaded materials, particularly those used for energy production. Different environmental conditions and genetic backgrounds shape embryogenesis. The robustness of embryogenesis in response to extrinsic and intrinsic changes remains incompletely understood. By analyzing the levels of two major nutrients, glycogen and neutral lipids, we discovered stage-dependent usage of these two nutrients along with mitochondrial morphology changes during *Caenorhabditis elegans* embryogenesis. ATGL, the rate-limiting lipase in cellular lipolysis, is expressed and required in the hypodermis to regulate mitochondrial function and support embryogenesis. The embryonic lethality of *atgl-1* mutants can be suppressed by reducing *sinh-1/age-1-akt* signaling, likely through modulating glucose metabolism to maintain sustainable glucose consumption. The embryonic lethality of *atgl-1(xd314)* is also affected by parental nutrition. Parental glucose and oleic acid supplements promote glycogen storage in *atgl-1(xd314)* embryos to compensate for the impaired lipolysis. The rescue by parental vitamin B12 supplement is likely through enhancing mitochondrial function in *atgl-1* mutants. These findings reveal that metabolic plasticity contributes to the robustness of *C. elegans* embryogenesis.

**Keywords** ATGL; embryogenesis; lipolysis; metabolic plasticity

**Subject Categories** Development; Metabolism

**DOI** 10.15252/embr.202357440 | Received 4 May 2023 | Revised 22 September 2023 | Accepted 11 October 2023 | Published online 27 October 2023

**EMBO Reports (2023) 24: e57440**

## Introduction

Robustness and plasticity are universal characteristics of biological systems when facing extrinsic and intrinsic changes (Kitano, 2004). Embryogenesis, a complex and energy-consuming process, is shaped by nutritional conditions and genetic alterations (Zhu *et al*, 2009; Paonessa *et al*, 2021; Rubio & Simon, 2021; Chen *et al*, 2022). The supply of nutrients during embryonic development

varies among species. In placental species, the embryo can continuously obtain nutrients from the mother through the placenta after implantation. In oviparous animals, the embryos wholly depend on maternally loaded nutrients. Embryonic nutrient reserves are shaped by maternal supply, which is affected by parental environmental conditions. Therefore, embryonic metabolism can be reshaped under changes in parental nutritional conditions. Changes in nutritional conditions may cause fetal maldevelopment and affect the expression of fetal genomes, thereby permanently altering the metabolism and physiology of offspring (Gardner *et al*, 2000; Wu *et al*, 2004).

Embryonic nutrient reserves usually consist of maternally loaded glycogen, lipids and amino acids (Ghosh *et al*, 2022). The efficient mobilization of nutrients provides energy as well as building blocks for cellular processes such as cell proliferation and morphogenesis. At different stages of embryonic development, embryos have a preference for utilizing certain nutrients. In humans, the fallopian tubes have higher pyruvate concentrations and lower glucose levels than the uterus. Thus, it is possible that the energy substrate preference of developing embryos is able to adapt to the different nutritional environments in the female reproductive tract (Scott *et al*, 2018). Embryos can also adjust to environmental changes. When cultured *in vitro*, the mouse embryo preferentially utilizes pyruvate as an energy substance in the early cleavage stage. At the morula stage, the consumption of pyruvate decreases, while the consumption of glucose increases sharply. However, in the absence of glucose in the medium, the consumption of pyruvate by mouse blastocysts is significantly increased (Gardner & Leese, 1988; Gardner *et al*, 2000).

Besides nutritional changes, embryogenesis also adapts to genetic alterations. For example, *C. elegans* embryos exhibit abnormal cell positioning and delayed cell division upon systematic knockdown of conserved genes. Interestingly, the timing of gene expression responds to the delayed cell proliferation, thereby coordinating the overall embryonic development process. The daughter cells returned to their normal position, and the embryos eventually hatched successfully (Xiao *et al*, 2022). Therefore, in the face of environmental and genetic perturbations, cellular plasticity and a variety of compensatory strategies help to mitigate or repair defects,

1 State Key Laboratory of Molecular Developmental Biology, Institute of Genetics and Developmental Biology, Chinese Academy of Sciences, Beijing, China

2 University of Chinese Academy of Sciences, Beijing, China

3 Tianjian Laboratory of Advanced Biomedical Sciences, Zhengzhou, China

\*Corresponding author. Tel: +86 10 64806560; E-mail: xhuang@genetics.ac.cn

increasing the robustness of embryonic development. However, the mechanisms that facilitate this robustness and plasticity to ensure normal embryonic development upon extrinsic or intrinsic changes remain incompletely understood.

The abundance and dynamics of neutral lipids in embryos vary greatly among different species (Dunning *et al*, 2014). Lipid droplets, the cellular neutral lipid storage organelles, are relatively small in mouse oocytes and early embryos, and gradually increase in size from the morula stage to blastocyst stage (Ibayashi *et al*, 2021; Mau *et al*, 2022). The size of lipid droplets reduces during embryonic diapause. Interestingly, there is a positive correlation between the abundance of neutral lipids in mammalian oocytes and the duration of diapause, which suggests that neutral lipids are consumed before implantation (Arena *et al*, 2021). The contribution of neutral lipid dynamics to embryonic development is not well understood. Lipase inhibitor treatment strongly inhibits zebrafish embryonic development, suggesting that lipolysis, which breaks down triacylglycerol (TAG) to glycerol and fatty acids, plays a key role in embryogenesis (Dutta & Sinha, 2017). Adipose triglyceride lipase (ATGL) is the rate-limiting enzyme responsible for cellular lipolysis (Zimmermann *et al*, 2004). *Drosophila* ATGL mutants are embryonic lethal (Gronke *et al*, 2005). However, the exact function of lipolysis during embryogenesis remains unclear. Furthermore, it is not known how embryos cope with lipolytic alterations.

*C. elegans* oogenesis occurs in the gonads. The mature oocytes are fertilized in the spermatheca. Then, the fertilized embryos form and are encased in the eggshell to begin the process of embryogenesis. Because *C. elegans* is transparent, we are able to observe multiple developing embryos in the uterus. In this study, we explored the mobilization of nutrients during *C. elegans* embryogenesis. We uncovered a differential usage of glycogen and triglycerides during embryogenesis. Based on the embryonic lethal phenotype caused by mutation of *atgl-1*, which encodes the sole ATGL homolog in *C. elegans*, we investigated the variability of *atgl-1* mutant phenotypes under different parental nutrient conditions and genetic backgrounds. Our results highlight the metabolic plasticity that ensures the robustness of *C. elegans* embryogenesis.

## Results

### A stage-dependent usage of glycogen and triglycerides during *C. elegans* embryogenesis

To characterize the mobilization of endogenous nutrient reserves during *C. elegans* embryogenesis, we analyzed the changes in glycogen and neutral lipid contents in oocytes and embryos. We measured glycogen content by iodine staining. Glycogen accumulates during oocyte maturation and reaches the highest level after fertilization. During embryonic development, glycogen content gradually decreases, indicating that glycogen is mobilized (Fig 1A and B; Appendix Fig S1A). Notably, glycogen appears to be depleted at the bean stage (Appendix Fig S1B). Compared to glycogen, neutral lipids, labeled by Bodipy dye, do not accumulate during oocyte maturation. The level of neutral lipids is increased after fertilization. In the early stage of embryogenesis, the lipid content is not greatly decreased (Fig 1C and D; Appendix Fig S1C). Starting from the gastrulation stage, lipid content drops sharply in most cells, indicating

active lipid mobilization. Intriguingly, the neutral lipid signal remains high in the hypodermal cells, labeled by a hypodermal marker  $P_{Y37A1B.5}::mCherry$  (Fig 1E and F).

As the ‘powerhouses’ of the cells, mitochondria adapt their activity to the requirements of cellular metabolism. The accumulation of the mitochondrial dye MitoTracker Red reflects mitochondrial membrane potential. Wild-type N2 embryos had weak MitoTracker Red staining at the early stage. As embryonic development proceeded, the intensity of staining greatly increased, indicating that the mitochondrial function gradually matured (Fig 1G). Nevertheless, there was no significant change in the relative mtDNA level between early and late embryos (Fig 1H). Notably, the transcription levels of genes related to mitochondrial fatty acid oxidation, including the acyl-CoA synthetase gene *acs-2* and the acyl-CoA dehydrogenase gene *C04E6.7*, were elevated in late embryos compared with early embryos (Fig 1I). Together, these results indicate that there is a differential usage of glycogen and neutral lipids during embryogenesis. In the early stages of development, the embryos mainly utilize glycogen; then, when the embryos are composed of dozens of cells, they start to mobilize neutral lipids. Moreover, the neutral lipids of hypodermal cells are mobilized later than those of other cell types.

### Glycogen and lipid mobilization are required for embryogenesis

To explore the role of glycogen and neutral lipid metabolism in embryogenesis, we examined the phenotypes of embryos carrying mutations in the *pygl-1*, *gsy-1*, and *atgl-1* genes, which encode key enzymes in glycogen or neutral lipid metabolism. *pygl-1* encodes a *C. elegans* homolog of mammalian PYGM, the rate-limiting enzyme in glycogen breakdown. *pygl-1(tm5211)*, a 915 bp deletion allele of *pygl-1*, results in increased embryonic glycogen content and an embryonic lethal phenotype when the parental *pygl-1(tm5211)* worms are grown under normal culture conditions (Fig 2A; Appendix Fig S1D). GSY-1 is the *C. elegans* homolog of the mammalian glycogen synthase GYS. *gsy-1(gk397885)*, a nonsense mutation allele of *gsy-1*, results in a significantly reduced glycogen content and a severe embryonic lethal phenotype when the parental *gsy-1(gk397885)* worms are grown under normal culture conditions (Fig 2A; Appendix Fig S1D). *pygl-1(tm5211)* and *gsy-1(gk397885)* mutant embryos developed into a few dozen cells and then died (Fig 2B), which suggests that glycogen metabolism is important for early embryonic development.

*atgl-1* is the *C. elegans* homolog of mammalian *Atgl*, encoding the rate-limiting TAG lipase in the cytosolic lipolysis pathway. Compared to N2, *atgl-1(xd314)*, a loss-of-function mutant, caused an increased level of neutral lipids in embryos especially in the hypodermis, by Bodipy staining (Fig 2C). In addition, *atgl-1(xd314)* mutants display an incomplete, but highly penetrant, embryonic lethal phenotype (Fig 2A and B). The embryonic lethality of *atgl-1(xd314)* can be rescued by fosmid transgenes containing wild-type *atgl-1*, which indicates that the phenotype was caused by the *atgl-1* mutation (Fig 2A). *lid-1* is a *C. elegans* homolog of mammalian CGI-58, an activator of ATGL (Lass *et al*, 2006; Xie & Roy, 2015b). *lid-1(xd288)* mutants also exhibit an embryonic lethal phenotype in *C. elegans* (Fig 2A).

To further characterize the embryonic lethal phenotype of *atgl-1(xd314)*, we used 4D imaging to track embryogenesis. *atgl-1(xd314)* embryos mainly died near the comma stage, around 390 min after

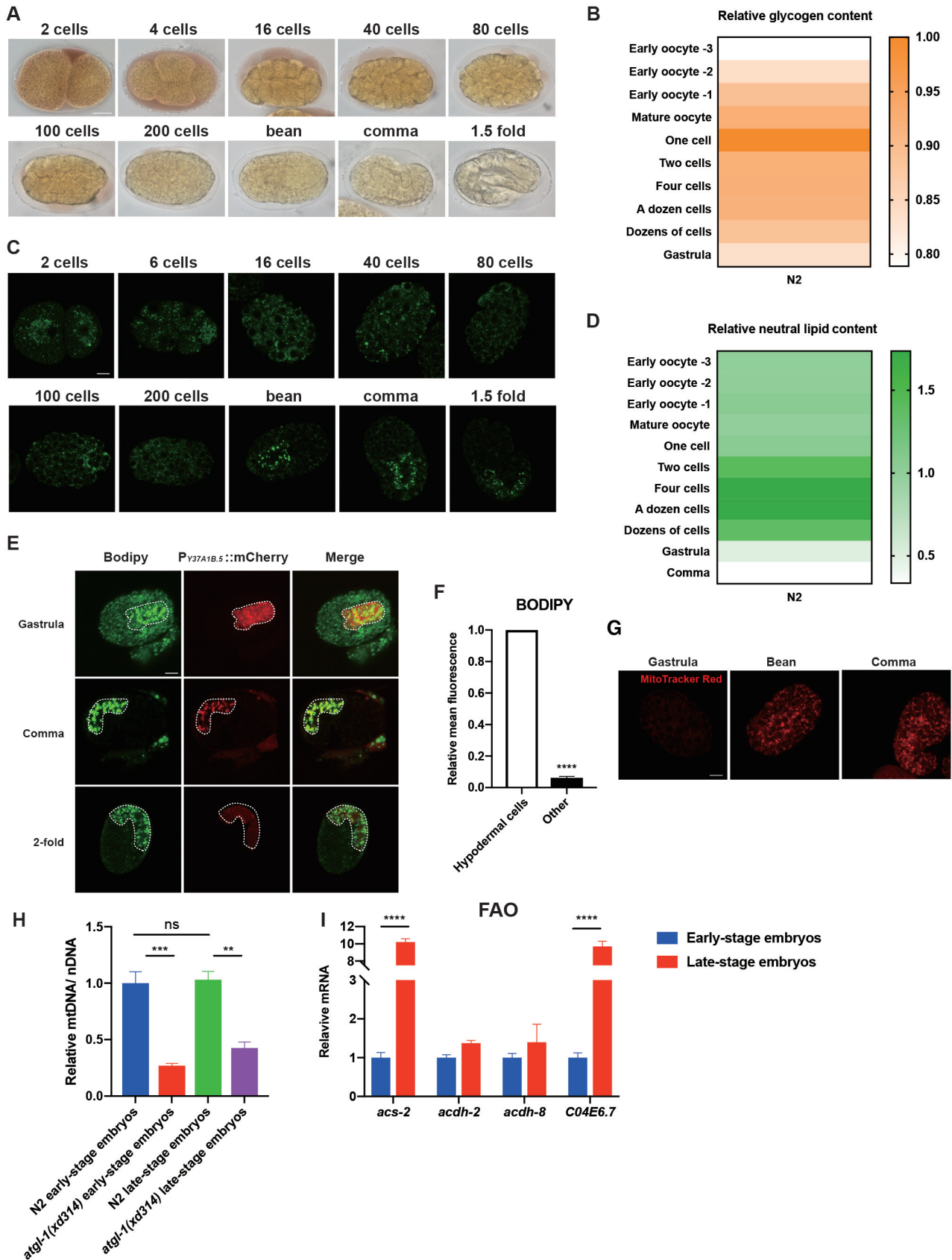


Figure 1.

**Figure 1. Differential usage of glycogen and neutral lipids during *C. elegans* embryogenesis.**

- A Iodine staining of N2 embryos at different stages. Scale bar: 10  $\mu$ m.
- B Quantification of the changes of glycogen content in oocytes and embryos of N2.  $n = 93$  embryos.
- C Bodipy staining of N2 embryos at different stages. Scale bar: 8  $\mu$ m.
- D Quantification of the changes of neutral lipid content in oocytes and embryos of N2.  $n = 95$  embryos.
- E Colabeling of cells by the hypodermal marker  $P_{Y37A1B.5}::mCherry$  and the lipid droplet dye Bodipy in N2 embryos. Scale bar: 8  $\mu$ m.
- F Quantification of the relative mean fluorescence density at the location of the hypodermal cells compared to the rest of the embryo in (E). Number of experiments  $n \geq 3$ , with at least 10 embryos analyzed in each experiment. The data were analyzed using two-way ANOVA. Data are presented as mean  $\pm$  SEM. \*\*\*\* $P < 0.0001$ .
- G MitoTracker Red staining of N2 embryos at different stages. Scale bar: 8  $\mu$ m.
- H The relative mtDNA/nDNA ratios of N2 and *atgl-1(xd314)* embryos at early and late stages. Three biological replicate samples were analyzed in this experiment. The data were analyzed using ordinary one-way ANOVA. Data are presented as mean  $\pm$  SEM. \*\* $P < 0.01$ , \*\*\* $P < 0.001$ ; ns: not significantly different.
- I The mRNA expression level of genes related to mitochondrial fatty acid oxidation including the acyl-CoA synthetase gene *acs-2*, and the acyl-CoA dehydrogenase genes *acdh-2*, *acdh-10*, and *C04E6.7*, in early and late stage N2 embryos. Four biological replicate samples were analyzed in this experiment. The data were analyzed using two-way ANOVA. Data are presented as mean  $\pm$  SEM. \*\*\*\* $P < 0.0001$ .

Source data are available online for this figure.

the first cleavage (Fig 2D). Ventral cleft closure and ventral enclosure are two major morphogenesis events before the comma stage: the former involves neuroblasts and the latter involves hypodermal cells. *atgl-1(xd314)* embryos exhibit aberrant ventral cleft closure and ventral enclosure (Fig 2D). The ventral clefts were larger and lasted longer in *atgl-1(xd314)* mutants than in N2 (Fig 2E and F). Many *atgl-1(xd314)* embryos eventually ruptured at the comma stage, which is a typical phenotype associated with defective ventral enclosure (Fig 2D). We used the adherens junction marker AJM-1::GFP to outline the hypodermal cells. This marker confirmed that ventral enclosure was defective in *atgl-1(xd314)* embryos (Fig 2G). Therefore, TAG hydrolysis is required for ventral morphogenesis.

**ATGL-mediated lipolysis in hypodermis supports embryogenesis**

We then investigated why the embryonic lethality of *atgl-1(xd314)* is incompletely penetrant. We quantified the cell proliferation and morphogenesis phenotypes of *atgl-1(xd314)* embryos at the single-cell level. Proliferation, cell cycle, and division asynchrony were investigated. For morphogenesis, the relative cell position was quantified during embryogenesis. There were no significant differences in the developmental phenotypes associated with proliferation between *atgl-1(xd314)* mutants and wild-type N2 before the 350-cell stage (Appendix Fig S2A and B). Before the AB128 stage, the cell positions in *atgl-1(xd314)* embryos were not much different from those of N2. After the AB128 stage, the number of abnormal cell

positions in *atgl-1(xd314)* embryos increased greatly (Appendix Fig S2C). The AB128 stage occurs about 190 min after fertilization, when the ventral cleft appears. Therefore, although *atgl-1(xd314)* embryos exhibit aberrant ventral cleft closure and hypodermal enclosure, embryonic development appears normal at earlier stages.

To identify the spatial requirement for ATGL-1 in embryogenesis, we performed tissue-specific rescue experiments. The morphogenesis events of ventral cleft closure and ventral enclosure involve neuroblasts and hypodermal cells. Overexpression of ATGL-1 in either the hypodermis or neurons partially rescued the embryonic lethality of *atgl-1(xd314)* (Fig 3A). Notably, the rescue activity in the hypodermis was higher than in neurons. In contrast, intestinal expression of ATGL-1 did not rescue *atgl-1(xd314)* (Fig 3A). In line with that, ATGL-1 appears to be expressed at a relatively high level in hypodermal cells after gastrulation based on the observation from a functional ATGL-1::GFP knockin reporter (Appendix Fig S2D). This result is supported by the observation that cells with high ATGL-1::GFP expression are colabeled with the hypodermal marker  $P_{Y37A1B.5}::mCherry$  (Fig 3B and C).

To determine whether *atgl-1* regulates embryonic neutral lipids autonomously or non-autonomously, we performed *atgl-1* tissue-specific knockout and *atgl-1* tissue-specific rescue experiments. *xdki26(loxP-atgl-1-loxP)*; *xdIs182(Prab-3::Cre)* is a neuronal-specific *atgl-1* knockout strain we previously generated (Yang et al, 2020). The neutral lipid levels in hypodermal cells of neuronal-specific *atgl-1* knockout embryos did not increase compared with wild-type

**Figure 2. Glycogen and neutral lipid mobilization are required for embryogenesis.**

- A The hatching rate of N2, *gsy-1(gk397885)*, *pygl-1(tm5211)*, *lid-1(xd288)*, *atgl-1(xd314)*, and *atgl-1(xd314); fosmid<sup>atgl-1</sup>. gsy-1(gk397885)*, *pygl-1(tm5211)*, *atgl-1(xd314)*, and *lid-1(xd288)* mutations lead to embryonic lethality in *C. elegans*. The embryonic lethality of *atgl-1(xd314)* can be rescued by fosmid transgenes containing wild-type *atgl-1*. Each dot represents one worm.  $n \geq 6$  worms for each genotype. The data were analyzed using ordinary one-way ANOVA. \*\*\*\* $P < 0.0001$ .
- B Nomarski differential interference contrast (DIC) images of *pygl-1(tm5211)*, *gsy-1(gk397885)*, and *atgl-1(xd314)* embryos. *pygl-1(tm5211)* and *gsy-1(gk397885)* embryos developed into a few dozen cells and then died. *atgl-1(xd314)* embryos ruptured around the bean and comma stages. Scale bar: 8  $\mu$ m.
- C Bodipy staining of N2 and *atgl-1(xd314)* embryos. The results show that levels of neutral lipids are increased in *atgl-1(xd314)* embryos, especially in the hypodermis. The red asterisks indicate the hypodermal cells. Scale bar: 25  $\mu$ m.
- D DIC images of N2 and *atgl-1(xd314)* embryos at different developmental stages. Compared with N2, *atgl-1(xd314)* embryos show an enlarged and persistent ventral cleft. The white dashed line outlines the ventral pocket. Scale bar: 5  $\mu$ m.
- E Quantification of the cleft size in (D). Number of experiments  $n \geq 3$ , with at least eight embryos per genotype analyzed in each experiment. The data were analyzed using unpaired t test. Data are presented as mean  $\pm$  SEM. \*\* $P < 0.01$ .
- F Quantification of the cleft duration in (D). Number of experiments  $n \geq 3$ , with at least eight embryos per genotype analyzed in each experiment. The data were analyzed using unpaired t test. Data are presented as mean  $\pm$  SEM. \*\* $P < 0.01$ .
- G The adherens junction marker AJM-1::GFP is used to outline the hypodermal cells. *atgl-1(xd314)* embryos show defective ventral hypodermal enclosure. The ventral pocket (marked by the white dashed line) cannot close in *atgl-1(xd314)* embryos. Scale bar: 10  $\mu$ m.

Source data are available online for this figure.



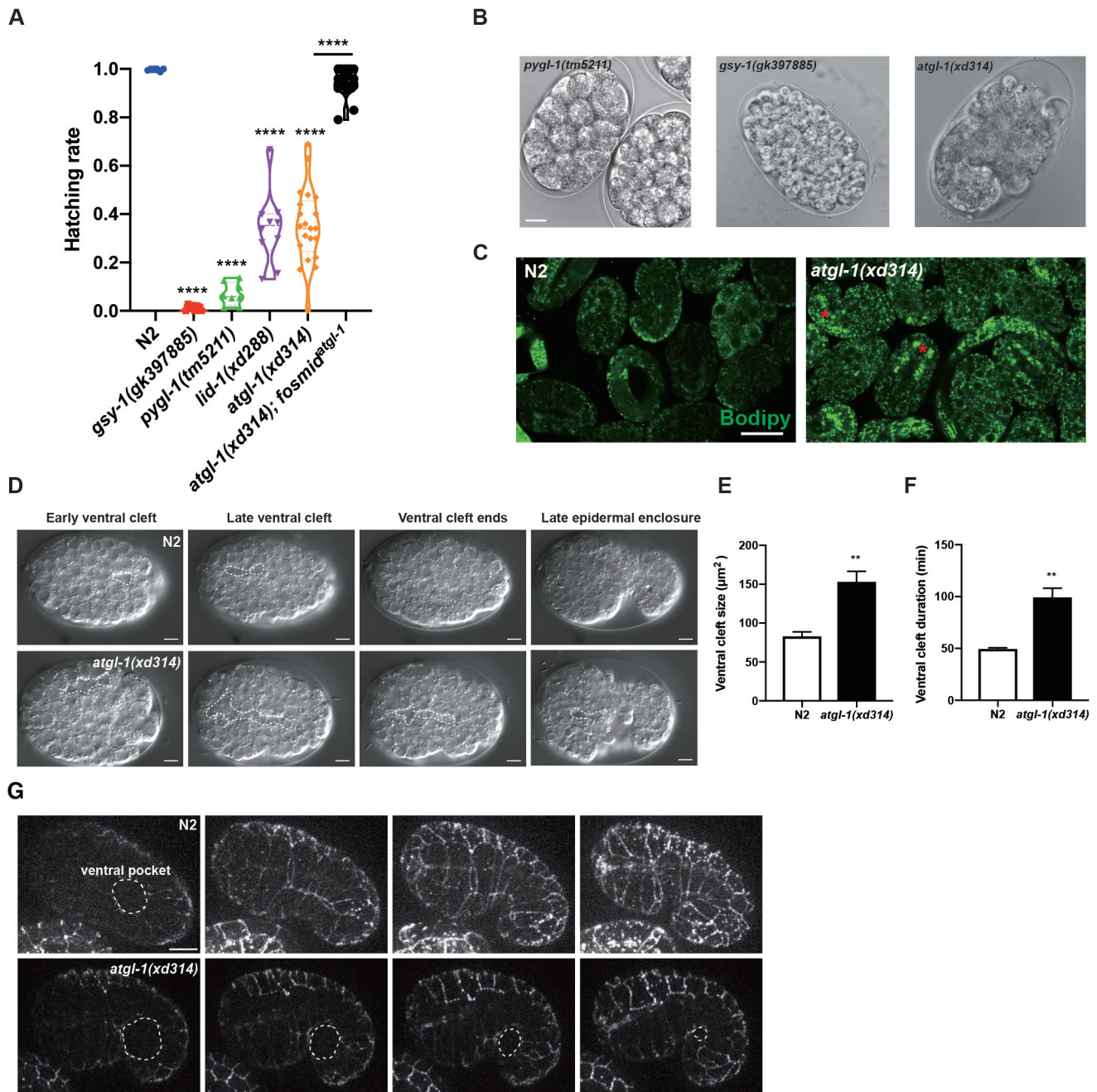


Figure 2.

N2 (Appendix Fig S2E and F). In addition, overexpression of ATGL-1 in hypodermis significantly reduced the high neutral lipid levels in *atgl-1(xd314)* hypodermal cells, but not in other cells (Appendix Fig S2E and F), indicating that ATGL-1 acts autonomously in hypodermal cells to hydrolyze TAG. Together, these results suggest that ATGL-1-mediated lipolysis in the hypodermis plays an important role in embryogenesis.

We also examined the mitochondrial morphology in hypodermis using a GFP reporter (Zhou et al., 2019). Based on the GFP pattern, we divided the morphology of mitochondria into three types: tubular, intermediate, and rod-shaped mitochondria (Fig 3D). The

hypodermal mitochondria exhibit a gradual transition from tubular to short rod-shaped during embryonic development (Movies EV1 and EV2). During the gastrulation stage, the mitochondria were mainly tubular, while in the bean and comma stages, the mitochondria were mainly rod shaped (Fig 3E and F). Compared to N2 embryos, *atgl-1(xd314)* embryos have fragmented mitochondria at the gastrulation stage (Fig 3E and F; Movie EV3). The mitochondria of *atgl-1(xd314)* embryos were spherical at the comma stage (Fig 3E and F; Movie EV4). The spherical mitochondria were not found in N2. In addition, the MitoTracker Red staining signal of *atgl-1(xd314)* embryos was

extremely low compared to wild-type N2 (Fig 3G), which suggests that *atgl-1* mutation impairs the function of mitochondria. Notably, the mtDNA/nDNA ratio was substantially reduced in *atgl-1* (*xd314*) embryos compared to wild type (Fig 1H), which further indicates that *atgl-1* mutation leads to mitochondrial dysfunction.

It has been reported that mitochondria can alter their morphology according to their proximity to lipid droplets (Benador et al, 2018). There was no significant difference in lipid droplet-mitochondria contacts between *atgl-1* RNAi L4 larvae and control RNAi L4 larvae (Appendix Fig S2G and H).

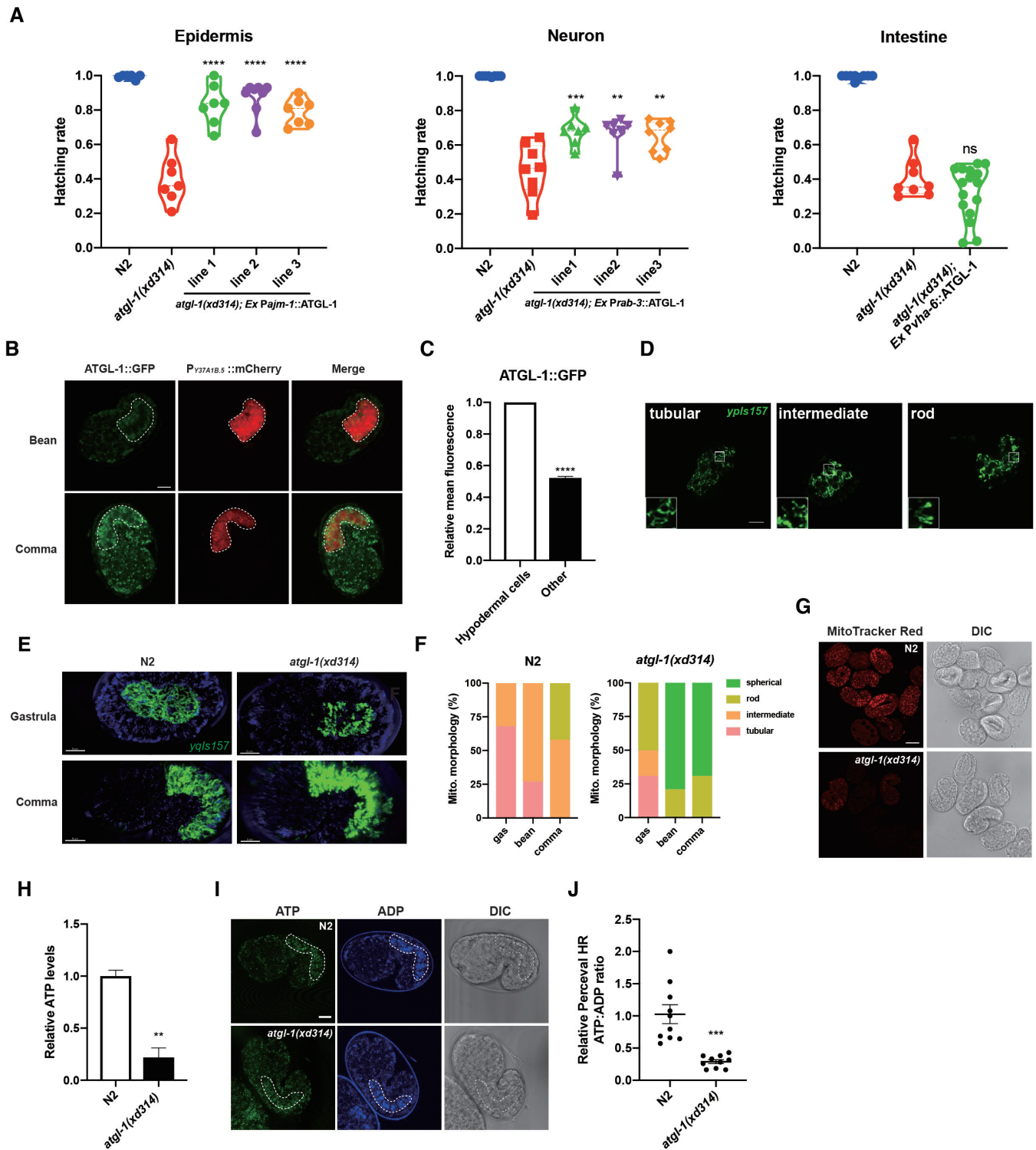


Figure 3.

**Figure 3. Hypodermal *atgl-1* is important for embryogenesis.**

- A The hatching rate of *atgl-1(xd314)*, *atgl-1(xd314); ExPajm-1::ATGL-1*, *atgl-1(xd314); ExPrab-3::ATGL-1*, and *atgl-1(xd314); ExPuha-6::ATGL-1*. Overexpression of ATGL-1 in hypodermis (left) or neurons (middle) rescues the embryonic lethality of *atgl-1(xd314)*, but intestinal overexpression (right) of ATGL-1 does not. Each dot represents one worm.  $n \geq 4$  worms for each genotype. The data were analyzed using ordinary one-way ANOVA. \*\* $P < 0.01$ , \*\*\* $P < 0.001$ , \*\*\*\* $P < 0.0001$ ; ns: not significantly different.
- B Colabeling of cells with the hypodermal marker  $P_{Y37A1B.5}::mCherry$  and the ATGL-1 reporter  $ATGL-1::GFP$  in N2 embryos. Scale bar: 8  $\mu m$ .
- C Quantification of the mean fluorescence density at the location of the hypodermal cells and in the rest of the embryo in (B). Number of experiments  $n \geq 3$ , with at least 10 embryos analyzed in each experiment. The data were analyzed using two-way ANOVA. Data are presented as mean  $\pm$  SEM. \*\*\*\* $P < 0.0001$ .
- D Images of mitochondria in embryonic hypodermal cells. The insets are enlarged views of the boxed areas. Based on their morphology, mitochondria are divided into three types: tubular, intermediate, and rod-shaped mitochondria. Scale bar: 8  $\mu m$ .
- E Images of mitochondria in embryonic hypodermal cells after 3D reconstruction. Mitochondria are colored in green and the rest of the embryo is colored in blue. Scale bar: 8  $\mu m$ .
- F Quantification of mitochondrial morphology in N2 and *atgl-1(xd314)*. Number of experiments  $n \geq 3$ , with at least 30 embryos per genotype analyzed in each experiment. Gas, gastrula.
- G MitoTracker Red staining of N2 and *atgl-1(xd314)* embryos. Scale bar: 20  $\mu m$ .
- H The ATP levels in N2 and *atgl-1(xd314)* embryos measured by ATP determination kit. Three biological replicate samples were analyzed in this experiment. The data were analyzed using Welch's t test. Data are presented as mean  $\pm$  SEM. \*\* $P < 0.01$ .
- I Images of PercevalHR, a genetically encoded ATP biosensor. PercevalHR was excited using 488 and 405 nm lasers corresponding to the ATP-bound and ADP-bound conformations, respectively. Scale bar: 8  $\mu m$ .
- J Quantification of the ATP:ADP ratio in (I). The ATP:ADP ratio in hypodermal cells is significantly reduced in *atgl-1(xd314)*. Number of experiments  $n \geq 3$ , with at least 10 embryos per genotype analyzed in each experiment. The data were analyzed using unpaired t test. \*\*\*\* $P < 0.0001$ .

Source data are available online for this figure.

It is possible that ATGL-1-mediated lipolysis might support morphogenesis by providing energy through mitochondrial oxidation. Compared to wild-type N2, ATP levels were significantly reduced in *atgl-1(xd314)* embryos measured by bioluminescence assay (Fig 3H). To specifically detect energy status in hypodermis, we tissue-specifically expressed PercevalHR, a genetically encoded ATP biosensor (Tantama et al, 2013). We found that the ATP:ADP ratio in hypodermal cells was significantly reduced in *atgl-1* mutants compared to wild-type control (Fig 3I and J). Therefore, an energy deficit may underlie the embryonic lethality of *atgl-1(xd314)* mutants and contribute to the incompletely penetrant phenotype.

### Reducing *sinh-1/age-1-akt* signaling rescues the embryonic lethality of *atgl-1* mutants

To uncover intrinsic mechanisms which may modulate the embryonic development of *atgl-1(xd314)* mutants, we performed a suppressor screen of *atgl-1(xd314)* (Appendix Fig S3A). Because of its low hatch rate, *atgl-1(xd314)* worms exhibited a slow food consumption rate. We screened for suppressor strains that consume the bacterial lawn more rapidly than *atgl-1(xd314)*. *xd342*, which harbors a 3,837 bp deletion at the *sinh-1* locus (Appendix Fig S3B), was discovered as a suppressor of *atgl-1(xd314)* embryonic lethality through SNP mapping and whole-genome sequencing. Fosmid transgenes carrying wild-type *sinh-1* were able to blunt the suppressive effect of *sinh-1(xd342)* (Fig 4A and B). In addition, *sinh-1(pe420)*, a frameshift mutant of *sinh-1*, also significantly suppressed the embryonic lethality of *atgl-1(xd314)* (Fig 4C). Notably, loss of function of *sinh-1* also rescued the embryonic lethal phenotype of *lid-1(xd288)* (Fig 4C). These results demonstrate that loss of function of *sinh-1* rescues embryonic lethality caused by impaired lipolysis.

*sinh-1/Sin1* is a key component of the mTORC2 complex (Fig 4A) (Yang et al, 2006). We constructed double mutants or performed RNAi on other mTORC2 components and downstream factors to examine whether they affect the hatching rate of *atgl-1(xd314)* embryos. *lst-8/LST8* and *rict-1/Rictor* are components of the

mTORC2 complex. *lst-8* RNAi rescued *atgl-1(xd314)* (Fig 4D). However, *rict-1* RNAi and mutation of *rict-1* cannot rescue *atgl-1(xd314)* (Fig 4D; Appendix Fig S3C). The downstream factors of mTORC2 include *sgk-1*, *pkc-1/2/3*, and *akt-1/2*. *pkc-3* RNAi is lethal, while the *sgk-1(ok538)* mutation cannot rescue *atgl-1(xd314)* (Appendix Fig S3D and E). There are two Akt genes in *C. elegans*, *akt-1* and *akt-2*. *akt-1(ok525)* and *akt-2(ok393)*, which are both loss-of-function alleles, failed to rescue *atgl-1(xd314)* separately (Appendix Fig S3F). To analyze whether *akt-1* and *akt-2* function redundantly, we generated *akt-1(ok525); akt-2(ok393); atgl-1(xd314)* triple mutants. However, the triple mutants undergo larval arrest, precluding the detailed analysis of embryogenesis. Therefore, we turned to *akt-1(mg144)*, a gain-of-function allele of *akt-1*. Notably, *akt-1(mg144)* abolished the suppressive effect of *sinh-1* on *atgl-1(xd314)* (Fig 4E), which indicates that Akt acts downstream of SINH-1 to mediate the suppression. Therefore, *sinh-1* mutation may rescue *atgl-1(xd314)* through the *sinh-1-akt* pathway.

The mTORC2 pathway intersects with the insulin pathway. In response to insulin stimulation, PI3K produces PIP3, which triggers the phosphorylation of Akt at Thr308 by PDK1. Akt then phosphorylates SIN1. Phosphorylated SIN1 promotes mTORC2 activity, which in turn promotes Akt activity via Ser473 phosphorylation (Liu et al, 2013; Yang et al, 2015; Yuan & Guan, 2015). AGE-1/PI3K is a central component of the insulin signaling pathway in *C. elegans* (Morris et al, 1996). Similar to *sinh-1* mutants, *age-1(hx546)*, a reduction-of-function allele of *age-1*, greatly suppressed the embryonic lethal phenotype of *atgl-1(xd314)* (Fig 4F). Conversely, a loss-of-function mutation in *daf-18/PTEN*, which antagonizes *age-1/PI3K* by dephosphorylating PIP3 to PIP2 (Ogg & Ruvkun, 1998), aggravated the embryonic lethal phenotype of *atgl-1(xd314)* (Fig 4G). Moreover, gain of function of *akt-1* abolished the suppressive effect of *age-1(hx546)* on *atgl-1(xd314)* (Fig 4F). *daf-2/IGFR* is an ortholog of human insulin/IGF-1 receptor in *C. elegans*, lying upstream of *age-1/PI3K* (Kimura et al, 1997). Mutation of *daf-2/IGFR* cannot rescue the embryonic lethal phenotype of *atgl-1(xd314)* (Fig 4H). Therefore, the suppressive effect of *age-1(hx546)* on *atgl-1(xd314)* may rely on some other descending input into



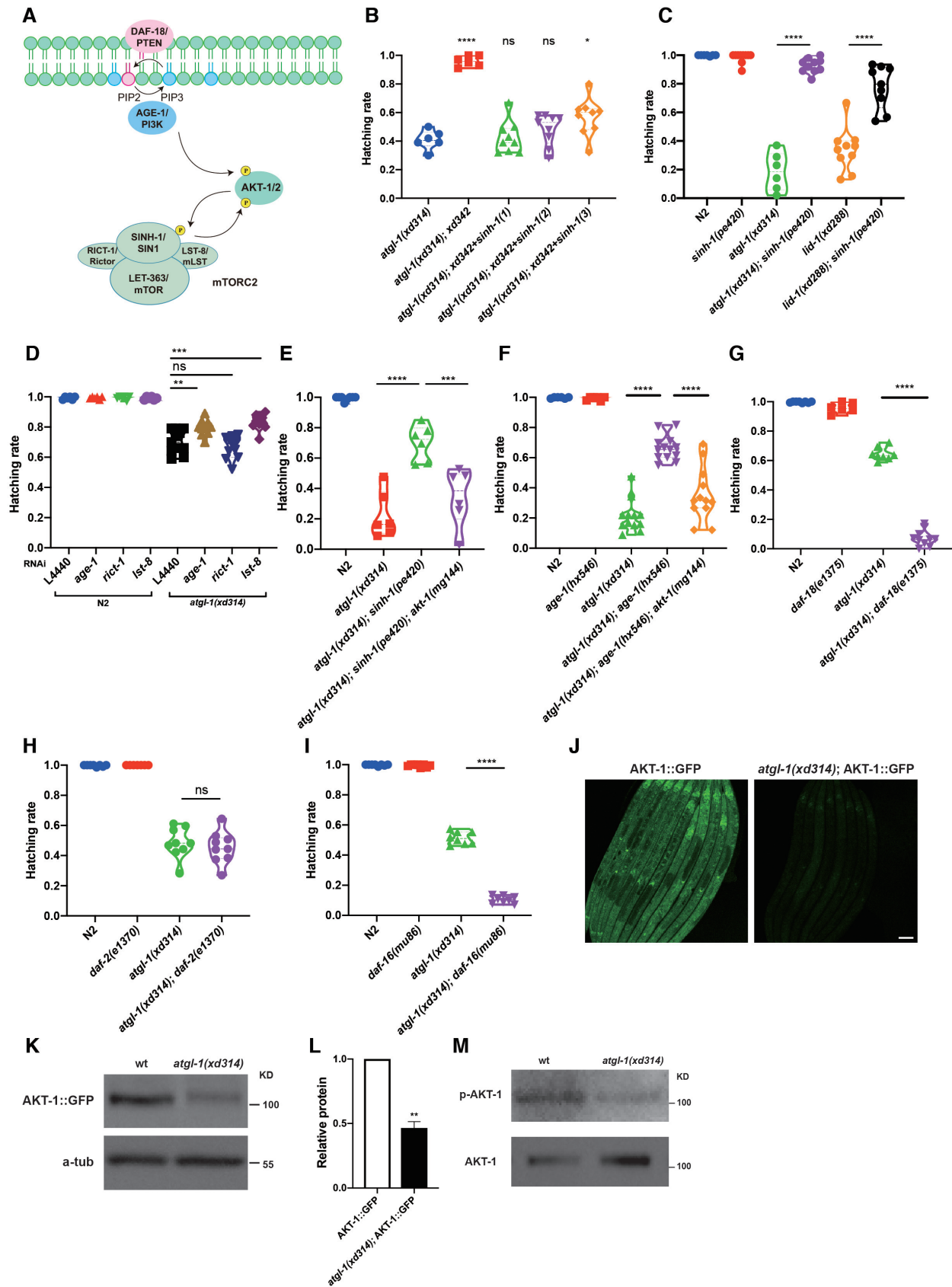


Figure 4.



**Figure 4. Reducing *sinh-1/age-1-akt* signaling rescues the embryonic lethality of *atgl-1* mutants.**

- A The *sinh-1/age-1-akt* signaling pathway in *C. elegans*.
- B The hatching rate of *atgl-1(xd314)*, *atgl-1(xd314); xd342* and *atgl-1(xd314); xd342; ExP<sub>sinh-1</sub>::SINH-1*. Fosmid transgenes containing wild-type *sinh-1* blunt the suppressive effect on *atgl-1(xd314)*; *sinh-1(xd342)*, indicating that *sinh-1* is a suppressor of *atgl-1(xd314)*. Each dot represents one worm.  $n \geq 6$  worms for each genotype. The data were analyzed using ordinary one-way ANOVA. \* $P < 0.05$ , \*\*\*\* $P < 0.0001$ ; ns: not significantly different.
- C The hatching rate of N2, *sinh-1(pe420)*, *atgl-1(xd314)*; *sinh-1(pe420)*, *lid-1(xd288)* and *lid-1(xd288); sinh-1(pe420)*. Loss of function of *sinh-1* strongly rescues the embryonic lethality of *atgl-1(xd314)* and *lid-1(xd288)*. Each dot represents one worm.  $n \geq 6$  worms for each genotype. The data were analyzed using ordinary one-way ANOVA. \*\*\*\* $P < 0.0001$ .
- D The hatching rate of *atgl-1(xd314)* and N2 when mTORC2 component genes are knocked down. *lst-8* RNAi alleviates the embryonic death of *atgl-1(xd314)*. Each dot represents one worm.  $n \geq 6$  worms for each RNAi. Since *E. coli* HT115 is an RNAi feeding strain, *atgl-1(xd314)* displayed a higher hatching rate in all RNAi control groups than when fed on the standard food *E. coli* OP50. The data were analyzed using ordinary one-way ANOVA. \*\* $P < 0.01$ , \*\*\* $P < 0.001$ ; ns: not significantly different.
- E The hatching rate of N2, *atgl-1(xd314)*, *atgl-1(xd314); sinh-1(pe420)* and *atgl-1(xd314); sinh-1(pe420); akt-1(mg144)*. Gain of function of *akt-1* abolishes the suppressive effect of *sinh-1* mutation on *atgl-1(xd314)*. Each dot represents one worm.  $n \geq 6$  worms for each genotype. The data were analyzed using ordinary one-way ANOVA. \*\*\*\* $P < 0.0001$ , \*\*\*\* $P < 0.0001$ .
- F The hatching rate of N2, *age-1(hx546)*, *atgl-1(xd314)*, *atgl-1(xd314); age-1(hx546)* and *atgl-1(xd314); age-1(hx546); akt-1(mg144)*. Gain of function of *akt-1* abolishes the suppressive effect of *age-1* mutation on *atgl-1(xd314)*. Each dot represents one worm.  $n \geq 6$  worms for each genotype. The data were analyzed using ordinary one-way ANOVA. \*\*\*\* $P < 0.0001$ .
- G The hatching rate of N2, *atgl-1(xd314)*, *daf-18(e1375)* and *atgl-1(xd314); daf-18(e1375)*. The *daf-18* mutation aggravates the embryonic lethal phenotype of *atgl-1(xd314)*. Each dot represents one worm.  $n \geq 6$  worms for each genotype. The data were analyzed using ordinary one-way ANOVA. \*\*\*\* $P < 0.0001$ .
- H The hatching rate of N2, *atgl-1(xd314)*, *daf-2(e1370)* and *atgl-1(xd314); daf-2(e1370)*. The *daf-2* mutation cannot rescue the embryonic lethal phenotype of *atgl-1(xd314)*. Each dot represents one worm.  $n \geq 7$  worms for each genotype. The data were analyzed using ordinary one-way ANOVA. ns: not significantly different.
- I The hatching rate of N2, *daf-16(mu86)*, *atgl-1(xd314)* and *atgl-1(xd314); daf-16(mu86)*. The *daf-16* mutation aggravates the embryonic lethal phenotype of *atgl-1(xd314)*. Each dot represents one worm.  $n \geq 8$  worms for each genotype. The data were analyzed using ordinary one-way ANOVA. \*\*\*\* $P < 0.0001$ .
- J Images of AKT-1::GFP in L4 worms of N2 and *atgl-1(xd314)*. AKT-1 is mainly expressed in the cytoplasm. Compared to control, the overall fluorescence of AKT-1::GFP is weak in *atgl-1(xd314)* mutants. Scale bar: 50  $\mu$ m.
- K The total amount of AKT-1::GFP, detected by western blot, is decreased in *atgl-1(xd314)* mutants. Three biological replicate samples were analyzed in this experiment.
- L Quantification of the western blot results of AKT-1::GFP in N2 and *atgl-1(xd314)*. Three biological replicate samples were analyzed in this experiment. The data were analyzed using Welch's *t* test. Data are presented as mean  $\pm$  SEM. \*\* $P < 0.01$ .
- M The level of phosphorylated AKT-1, detected by western blot, is decreased in *atgl-1(xd314)* mutants.
- Source data are available online for this figure.

PI3K signaling. The forkhead type transcription factor DAF-16/FOXO governs major functions of insulin signaling in *C. elegans* (Lin et al, 1997; Ogg et al, 1997). Activation of the insulin pathway inhibits DAF-16 activity through reducing its nuclear localization (Gottlieb & Ruvkun, 1994). Loss of function of *daf-16* aggravated the *atgl-1(xd314)* embryonic lethal phenotype (Fig 4I). This indicates that upregulating the activity of the insulin signaling pathway will exacerbate the embryonic lethality of *atgl-1(xd314)*.

We also examined the localization of DAF-16::GFP during embryonic development. DAF-16::GFP was expressed from the bean stage and was mainly localized in the nucleus at the comma stage and the 1.5-fold stage. In embryos after the 1.5-fold stage, DAF-16::GFP showed obvious cytosolic localization (Appendix Fig S3G). The localization of DAF-16::GFP was not changed in *atgl-1(xd314)* mutants. Notably, *sinh-1(pe420)* and *age-1(hx546)* mutations led to nuclear localization of DAF-16::GFP even after the 1.5-fold stage (Appendix Fig S3G), consistent with the fact that *sinh-1* and *age-1* mutations reduce the insulin pathway activity in *C. elegans*. Moreover, the localization of DAF-16::GFP in *atgl-1(xd314)*; *sinh-1(pe420)* and *atgl-1(xd314)*; *age-1(hx546)* double mutants is the same as *sinh-1(pe420)* and *age-1(hx546)* single mutants, respectively.

To further decipher the link between *sinh-1/age-1-akt* signaling and *atgl-1*, we examined the activity of the *sinh-1/age-1-akt* pathway. The genetic suppression raises the possibility that *sinh-1/age-1-akt* signaling is increased in *atgl-1(xd314)* mutants. We used a functional AKT-1::GFP knockin reporter to examine the levels of AKT and phosphorylated AKT. Interestingly, the overall level of AKT-1::GFP, determined by both fluorescence intensity and western

blot assay, was reduced in *atgl-1(xd314)* (Fig 4J–L). Moreover, the ratio of phosphorylated/total AKT-1 was decreased in *atgl-1(xd314)* (Fig 4M). This suggests that the activity of the *sinh-1/age-1-akt* pathway was already reduced in *atgl-1(xd314)* mutants, probably due to a compensatory effect. We also explored the transcriptional regulation of *akt-1* with a *Pakt-1::GFP* reporter. The GFP fluorescent signal was not reduced in *atgl-1(xd314)* (Appendix Fig S3H). Put together, these results indicate that reduction of the *sinh-1/age-1-akt* signal represents an intrinsic metabolic plasticity in *atgl-1(xd314)*.

#### The suppressive effect of *sinh-1/age-1-akt* signaling reduction on *atgl-1* mutants depends on glucose metabolism

We next investigated the underlying mechanism of the suppressive effect of *sinh-1/age-1-akt* signaling reduction. We investigated whether *age-1* and *sinh-1* mutations rescue the mitochondrial defects of *atgl-1(xd314)*. The mitochondrial fragmentation phenotype of *atgl-1(xd314)* embryos persisted in *atgl-1(xd314)*; *age-1(hx546)* and *atgl-1(xd314)*; *sinh-1(pe420)* double mutants (Appendix Fig S4A and B). Therefore, the suppressive effect of *age-1* and *sinh-1* mutations on *atgl-1(xd314)* is probably not mediated through improving mitochondrial function.

The *sinh-1/age-1-akt* pathway regulates both glucose and lipid homeostasis (Lamming & Sabatini, 2013; Kim & Guan, 2019; Liu & Sabatini, 2020). We explored whether downregulation of the *sinh-1/age-1-akt* signaling pathway alleviates the embryonic lethality of *atgl-1(xd314)* through promoting the utilization of neutral lipids or by affecting glucose metabolism. Compared with N2, the neutral lipid content was greatly increased in *atgl-1(xd314)* embryos.

However, *age-1* mutation did not significantly reduce the high embryonic lipid levels caused by *atgl-1* mutation (Fig 5A). We also examined neutral lipid levels in adults. Consistent with previous reports (Narbonne & Roy, 2009; Lee et al, 2014; Xie & Roy, 2015a, 2015b), Oil Red O staining revealed that the *atgl-1* mutation significantly increased the lipid content under fed conditions. In addition, the lipid content of N2 decreased gradually with prolonged

starvation, while *atgl-1(xd314)* mutants exhibited lipid mobilizing defects and the lipid content did not decrease with starvation (Appendix Fig S4C and D). Neither the *age-1* mutation nor the *sinh-1* mutation reduced the lipid content of *atgl-1(xd314)* mutants under fed or starved conditions (Appendix Fig S4C and D). Furthermore, it was reported that loss-of-function *age-1* or *sinh-1* leads to increased body fat in larvae or adult worms (Ogg & Ruvkun, 1998; Hansen

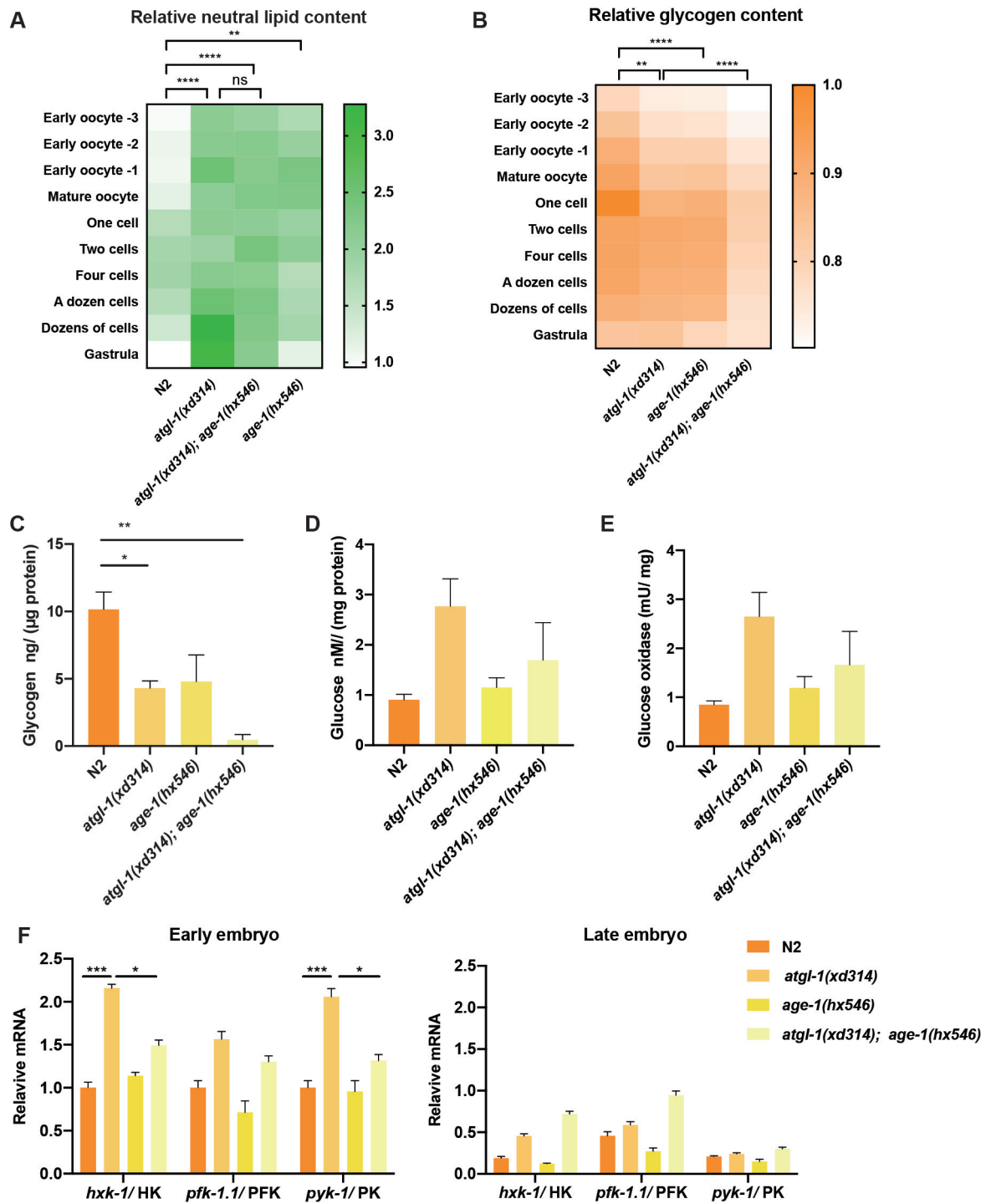


Figure 5.

**Figure 5. The suppressive effect of *sinh-1/age-1-akt* signaling reduction on *atgl-1* mutants depends on glucose metabolism.**

- A Quantification of Bodipy staining results of oocytes and embryos of N2, *atgl-1(xd314)*, *atgl-1(xd314); age-1(hx546)* and *age-1(hx546)*. *age-1* mutation does not significantly reduce the high embryonic lipid levels in *atgl-1(xd314)* embryos.  $n \geq 67$  embryos for each group. The data were analyzed using two-way ANOVA.  $**P < 0.01$ ,  $****P < 0.0001$ ; ns: not significantly different.
- B Quantification of iodine staining results of oocytes and embryos of N2, *atgl-1(xd314)*, *atgl-1(xd314); age-1(hx546)* and *age-1(hx546)*. *age-1* mutation further reduces the glycogen content in *atgl-1(xd314)* embryos. The data were analyzed using two-way ANOVA.  $**P < 0.01$ ,  $****P < 0.0001$ .
- C Glycogen levels in N2, *atgl-1(xd314)*, *age-1(hx546)* and *atgl-1(xd314); age-1(hx546)* embryos, measured by a glycogen colorimetric assay kit. *age-1* mutation further reduces the glycogen content in *atgl-1(xd314)* embryos. The total amount of glycogen was normalized to the total protein in the sample. Three biological replicate samples were analyzed in this experiment. The data were analyzed using ordinary one-way ANOVA. Data are presented as mean  $\pm$  SEM.  $*P < 0.05$ ,  $**P < 0.01$ .
- D Glucose levels in N2, *atgl-1(xd314)*, *age-1(hx546)* and *atgl-1(xd314); age-1(hx546)* embryos measured by an Invitrogen™ Amplex™ Red glucose assay kit. The glucose content is elevated in *atgl-1(xd314)* embryos. The total amount of glucose was normalized to the total protein in the sample. Three biological replicate samples were analyzed in this experiment. The data were analyzed using ordinary one-way ANOVA. Data are presented as mean  $\pm$  SEM.
- E The glucose oxidase activity in N2, *atgl-1(xd314)*, *age-1(hx546)* and *atgl-1(xd314); age-1(hx546)* embryos measured by an Invitrogen™ Amplex™ Red glucose oxidase assay kit. The glucose oxidase activity is elevated in *atgl-1(xd314)* embryos. Three biological replicate samples were analyzed in this experiment. The data were analyzed using ordinary one-way ANOVA. Data are presented as mean  $\pm$  SEM.
- F The mRNA expression level of glycolytic enzymes in N2, *atgl-1(xd314)*, *age-1(hx546)*, and *atgl-1(xd314); age-1(hx546)* early-stage and late-stage embryos. The transcription levels of genes encoding key enzymes in the glycolysis pathway are generally upregulated in *atgl-1(xd314)* embryos. Three biological replicate samples were analyzed in this experiment. The data were analyzed using two-way ANOVA. Data are presented as mean  $\pm$  SEM.  $*P < 0.05$ ,  $****P < 0.001$ .

Source data are available online for this figure.

et al, 2005; Sakai et al, 2017). Therefore, it is unlikely that *age-1* and *sinh-1* mutants alleviate the embryonic lethal phenotype of *atgl-1(xd314)* through increasing lipid mobilization.

Next, we investigated whether the *sinh-1/age-1-akt* pathway affects *atgl-1(xd314)* embryonic development through glucose metabolism. In *atgl-1(xd314)* embryos, the glycogen content is significantly reduced compared to wild type (Fig 5B). On the other hand, glucose content was increased in *atgl-1(xd314)* embryos (Fig 5B–D). In addition, glucose oxidase activity was elevated in *atgl-1(xd314)* embryos and the transcription levels of key enzymes in the glycolysis pathway were also generally upregulated (Fig 5E and F; Appendix Fig S4E). These observations suggest that excess glycogen is mobilized and glucose utilization is significantly increased to compensate for the loss of lipolysis in *atgl-1(xd314)* embryos. The insulin–AKT signal promotes glucose metabolism through increasing the activity of glycogen synthesis and glycolysis pathways (Titchenell et al, 2017). In line with this, the glycogen content was reduced in *age-1(hx546)* mutants (Fig 5B and C). *age-1* mutation further reduced the glycogen content in *atgl-1(xd314)* embryos, while maintaining high embryonic glucose levels (Fig 5B–D). Compared with *atgl-1(xd314)* embryos, the glucose oxidase activity in *atgl-1(xd314); age-1(hx546)* embryos tended to decrease (Fig 5E). Indeed, the transcription levels of glycolytic enzymes are significantly higher in early embryos than in late embryos (Fig 5F). Furthermore, the transcription levels of key glycolytic enzymes were generally downregulated in *atgl-1(xd314); age-1(hx546)* compared with *atgl-1(xd314)* embryos (Fig 5F). Additionally, the transcription levels of *pygl-1* had an upregulated trend in *age-1(hx546)* and *atgl-1(xd314); age-1(hx546)* (Appendix Fig S4F). These results suggest that *age-1* mutation may help to maintain the sustainable consumption of glucose to cope with the energy deficit of *atgl-1* mutants.

#### Parental glucose and oleic acid supplements promote glycogen storage in *atgl-1(xd314)* embryos to overcome impaired lipolysis

The above genetic suppressions prompted us to explore whether the embryonic phenotype of *atgl-1* mutants is also affected by extrinsic nutritional changes. Parental worms were cultured on plates containing extra glucose or oleic acid, and the progeny were

analyzed. Parental glucose and oleic acid supplements alleviated the embryonic lethal phenotype of *atgl-1(xd314)* (Fig 6A and B). Interestingly, both treatments increased the glycogen storage in both N2 and *atgl-1(xd314)* embryos (Fig 6C and D), while the lipid content in the embryos was not significantly changed (Appendix Fig S5A). Moreover, parental glucose supplementation slightly alleviated mitochondrial fragmentation in *atgl-1(xd314)* embryos (Fig 6E). In contrast, parental oleic acid supplementation did not change the mitochondrial fragmentation phenotype of *atgl-1(xd314)* (Fig 6F). Notably, the rescuing effect of oleic acid supplement is better than glucose supplement, despite similarly increased levels of glycogen. Therefore, the suppression of embryonic lethality through parental glucose and oleic acid supplementation is probably not mediated through rescue of the mitochondrial defects or through increasing lipid mobilization.

To investigate whether the suppressive effect of parental glucose and oleic acid supplements depend on glucose metabolism, we knocked down *gsy-1* and *pygl-1* under the conditions of glucose and oleic acid supplement. We found that knockdown of *gsy-1* and *pygl-1* eliminated the suppressive effect of parental glucose and oleic acid supplements, which suggests that the suppressive effect of these parental supplements depends on glucose metabolism (Fig 6G and H).

#### Parental vitamin B12 supplement rescues the mitochondrial defects and embryonic lethality of *atgl-1(xd314)*

The embryonic lethal phenotype of *atgl-1(xd314)* was observed under standard culture conditions: the parental animals were well fed with *E. coli* OP50. We accidentally discovered that the incompletely penetrant embryonic lethality phenotype is dramatically affected by the culture condition. The lethality of *atgl-1(xd314)* embryos was significantly alleviated when the parental animals were cultured with HT115, an *E. coli* strain usually used for RNAi (Fig 7A).

*E. coli* HT115 contains more vitamin B12 than OP50 (Revtovich et al, 2019). Vitamin B12 supplementation increases mitochondrial biogenesis and connectivity in *C. elegans* (Wei & Ruvkun, 2020). In line with this, HT115 feeding rescued the fragmented mitochondrial

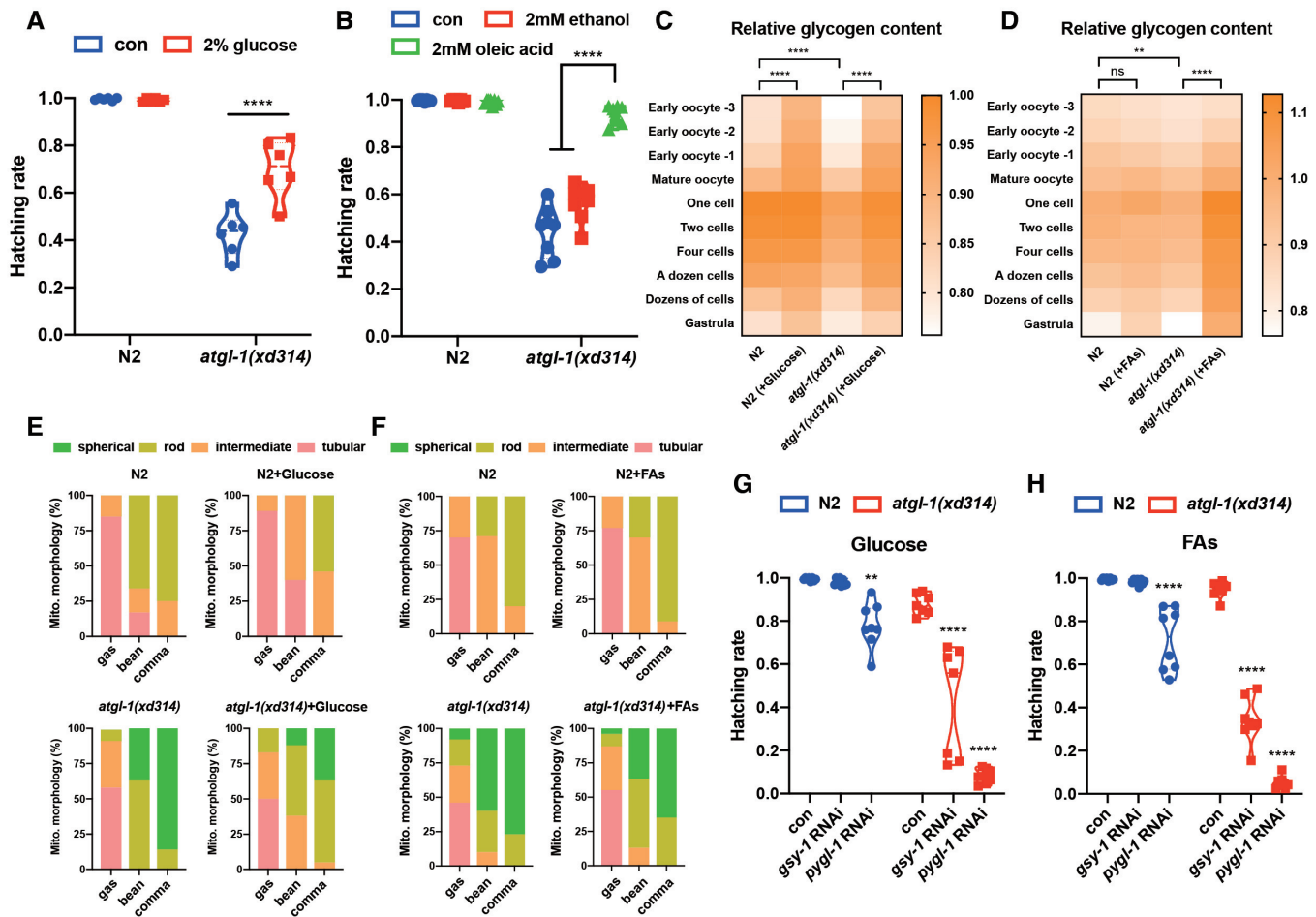


**Figure 6. Parental glucose and oleic acid supplements promote glycogen storage in *atgl-1(xd314)* embryos to overcome impaired lipolysis.**

- A The hatching rate of *atgl-1(xd314)* and N2 when the parental worms were fed on *E. coli* OP50 on regular medium (NGM) or OP50 on NGM + 2% glucose. Glucose feeding alleviates the lethal phenotype of *atgl-1(xd314)* embryos. Each dot represents one worm.  $n \geq 6$  worms for each genotype. The data were analyzed using two-way ANOVA. \*\*\*\* $P < 0.0001$ .
- B The hatching rate of *atgl-1(xd314)* and N2 when the parental worms were fed on *E. coli* OP50 on regular NGM plates or OP50 on NGM + 2 mM oleic acid. The addition of oleic acid to the medium increases the hatching rate of *atgl-1(xd314)* mutant embryos. Oleic acid was dissolved in ethanol. Each dot represents one worm.  $n = 8$  worms for each genotype. The data were analyzed using two-way ANOVA. \*\*\*\* $P < 0.0001$ .
- C Quantification of iodine staining results of oocytes and embryos of N2 and *atgl-1(xd314)*. The glycogen content in *atgl-1(xd314)* embryos is significantly reduced. Parental glucose feeding promotes the accumulation of glycogen in embryos of N2 and *atgl-1(xd314)*.  $n \geq 78$  embryos for each group. The data were analyzed using two-way ANOVA. \*\*\*\* $P < 0.0001$ .
- D Quantification of iodine staining results of oocytes and embryos of N2 and *atgl-1(xd314)* when the parental worms were fed on plates with exogenous fatty acid. Fatty acid feeding promotes glycogen accumulation in *atgl-1(xd314)* embryos.  $n \geq 126$  embryos for each group. The data were analyzed using two-way ANOVA. \*\* $P < 0.01$ , \*\*\*\* $P < 0.0001$ ; ns: not significantly different.
- E Quantification of mitochondrial morphology in N2 and *atgl-1(xd314)* embryos when the parental worms were fed on plates with exogenous glucose. Glucose feeding slightly alleviates the mitochondrial fragmentation in *atgl-1(xd314)* embryos. Number of experiments  $n \geq 3$ , with at least 30 embryos per genotype analyzed in each experiment. Gas, gastrula.
- F Quantification of mitochondrial morphology in N2 and *atgl-1(xd314)* embryos when the parental worms were fed with exogenous oleic acid. The addition of oleic acid did not alleviate the mitochondrial fragmentation phenotype of *atgl-1(xd314)* mutants. Number of experiments  $n \geq 3$ , with at least 30 embryos per genotype analyzed in each experiment. Gas, gastrula.
- G The hatching rate of *atgl-1(xd314)* and N2 with knockdown of *gsy-1* and *pygl-1* upon glucose feeding. *gsy-1* and *pygl-1* RNAi eliminate the suppressive effect of parental glucose supplement. Each dot represents one worm.  $n \geq 7$  worms for each genotype. The data were analyzed using two-way ANOVA. \*\* $P < 0.01$ , \*\*\*\* $P < 0.0001$ .
- H The hatching rate of *atgl-1(xd314)* and N2 with knockdown of *gsy-1* and *pygl-1* upon oleic acid feeding. *gsy-1* and *pygl-1* RNAi remove the suppressive effect of parental oleic acid supplement. Each dot represents one worm.  $n \geq 7$  worms for each genotype. The data were analyzed using two-way ANOVA. \*\*\*\* $P < 0.0001$ .

Source data are available online for this figure.

phenotype of *atgl-1(xd314)* (Fig 7B and C). We then investigated whether the vitamin B12 difference between OP50 and HT115 explains the beneficial effect of HT115 on *atgl-1(xd314)*. We added

vitamin B12 to the OP50 medium. Parental vitamin B12 supplement increased mitochondrial fusion at various embryonic stages in both N2 and *atgl-1(xd314)* (Fig 7B and C). Importantly, parental vitamin



B12 supplement partially restored the mitochondrial membrane potential of *atgl-1(xd314)* and reduced the embryonic lethality of *atgl-1(xd314)* (Fig 7D and E). Furthermore, we examined the effect

of vitamin B12 supplementation on the neutral lipid content of embryos. The high neutral lipid content in *atgl-1(xd314)* embryos slightly decreased when vitamin B12 was added (Appendix

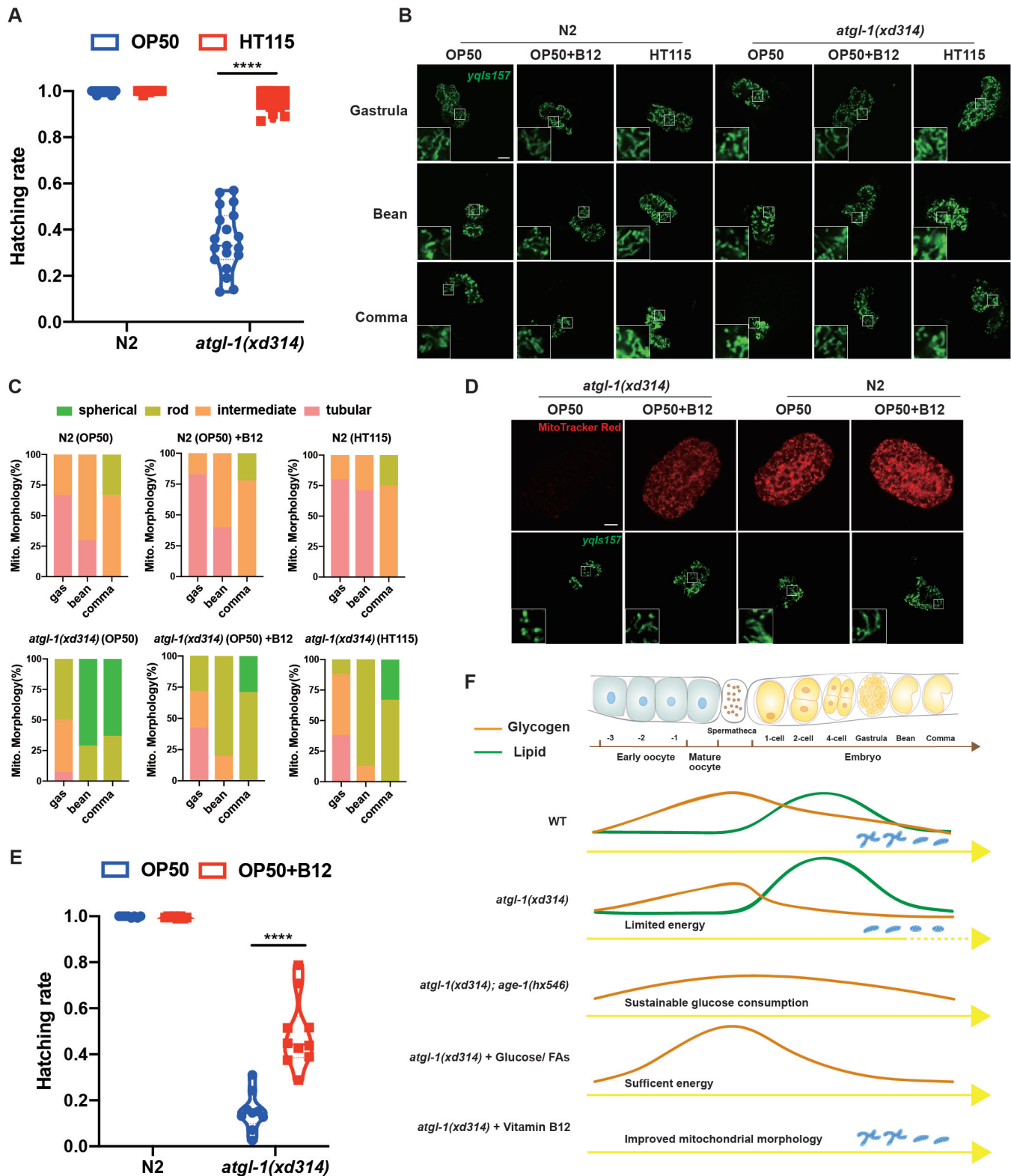


Figure 7.

**Figure 7.** Parental vitamin B12 supplement rescues the mitochondrial defects and embryonic lethality of *atgl-1(xd314)*

- A The hatching rate of *atgl-1(xd314)* and N2 embryos when the parental worms were fed on *E. coli* OP50 or HT115. HT115 feeding alleviates embryonic death caused by *atgl-1* mutation. Each dot represents one worm.  $n \geq 19$  worms for each genotype. The data were analyzed using two-way ANOVA. \*\*\*\* $P < 0.0001$ .
- B Images of mitochondria in embryonic hypodermal cells when the worms were fed on the indicated bacteria without or with B12 supplement. The insets are enlarged views of the boxed areas. *E. coli* HT115 (unsupplemented) and OP50 supplemented with vitamin B12 increase mitochondrial fusion at various embryonic stages in both N2 and *atgl-1(xd314)*. Scale bar: 8  $\mu\text{m}$ .
- C Quantification of mitochondrial morphology in (B). Gas, gastrula.
- D MitoTracker Red staining and mitochondrial marker *yqj157* (green) in N2 and *atgl-1(xd314)* embryos. The insets are enlarged views of the boxed areas. Parental vitamin B12 supplement increases mitochondrial fusion and partially restores the mitochondrial membrane potential of *atgl-1(xd314)* embryos. Scale bar: 8  $\mu\text{m}$ .
- E The hatching rate of N2 and *atgl-1(xd314)* when the parental worms were supplemented with exogenous vitamin B12. Vitamin B12 alleviates embryonic death caused by *atgl-1* mutation.  $n \geq 8$  worms for each genotype. The data were analyzed using ordinary one-way ANOVA. \*\*\*\* $P < 0.0001$ .
- F Model showing how multiple metabolic plasticity strategies contribute to the robustness of *C. elegans* embryogenesis. At the top of the model is a diagram showing the developmental timeline of oogenesis and embryogenesis in an adult hermaphrodite. Left, oocytes at different stages of development (blue shading) in the gonad; middle, sperm (orange dots) in the spermatheca; right: embryos at different stages of development (yellow shading) in the uterus. Glycogen continuously accumulates during oocyte maturation, whereas neutral lipid accumulation is not initiated until after fertilization. In the early stage of embryonic development, the embryo first uses glycogen as an energy source. When the embryo comprises dozens of cells, it begins to mobilize lipids to provide energy for further development. The *atgl-1* mutation leads to increased neutral lipid content and reduced glycogen content in embryos. Hypodermal mitochondria undergo a transition from filamentous to short rod-shaped morphology during *C. elegans* embryogenesis. When *atgl-1* is mutated, mitochondria become more fragmented, and morphological transitions are advanced. Endogenous regulation of *sinh-1/age-1-akt* signaling may rescue the phenotype of *atgl-1(xd314)* embryos by promoting the sustainable consumption of glucose. The *atgl-1(xd314)* phenotype can also be rescued by promoting glycogen accumulation through addition of exogenous nutrients, such as glucose and fatty acids, to the food of the parental worms. In addition, parental vitamin B12 supplement alleviates the mitochondrial defects and embryonic lethality of *atgl-1(xd314)*.

Source data are available online for this figure.

Fig S5A). This decrease may be due to elevated lipid mobilization since the addition of vitamin B12 partially restored the mitochondrial function of *atgl-1(xd314)*.

Besides regulating mitochondrial morphology, vitamin B12, as a coenzyme, is also involved in cellular propionic acid degradation, the one-carbon cycle pathway and phosphatidylcholine (PC) synthesis (Zhu *et al*, 2022, 2023). To determine whether vitamin B12 supplementation affects the embryonic development of *atgl-1(xd314)* through these pathways, we knocked down genes encoding key enzymes for propionic acid degradation (*mmcm-1*), one-carbon cycle (*metr-1/mtrr-1*, *sams-3/4/5*) and PC synthesis (*cept-2*) under the condition of vitamin B12 supplementation to examine whether the hatching rate of *atgl-1(xd314)* was affected. We found that *mmcm-1* and *metr-1/mtrr-1* RNAi did not affect the hatching rate of *atgl-1(xd314)* (Appendix Fig S5B). *cept-2* RNAi significantly reduced the hatching rate of *atgl-1(xd314)* (Appendix Fig S5B). However, *cept-2* RNAi also caused embryonic death in the wild-type N2 background (Appendix Fig S5B). Collectively, these results suggest that vitamin B12 supplementation rescues the embryonic lethality of *atgl-1(xd314)* mainly by affecting the mitochondrial morphology of *atgl-1(xd314)* embryos.

Together, these results show that the embryonic lethality of *atgl-1(xd314)* can be suppressed by extrinsically supplying glucose, oleic acid, or vitamin B12 to the parental worms. The rescuing effects of various parental nutrient supplements suggest that embryogenesis displays metabolic plasticity in response to changes in the culture conditions of the parental worms. In summary, the metabolic robustness and plasticity of *C. elegans* embryogenesis are supported by metabolic changes during embryogenesis and the variability of *atgl-1(xd314)* mutant phenotypes under different parental nutrient conditions and genetic backgrounds.

## Discussion

The mechanisms that facilitate robust embryogenesis in response to genetic and environmental metabolic perturbations remain obscure.

Starting from the observation of an embryonic stage-dependent usage of glycogen and neutral lipids, we identified the important function of hypodermal lipolysis in embryogenesis. The embryonic lethality of *atgl-1(xd314)* mutants can be rescued by intrinsic down-regulation of the *sinh-1/age-1-akt* signaling pathway or parental supplementation with extrinsic nutrients (Fig 7F). These results demonstrate metabolic plasticity, which ensures the robustness of *C. elegans* embryogenesis.

Mitochondrial function and morphology are impaired and neutral lipids are not efficiently mobilized in *atgl-1(xd314)* embryos. The relatively high hypodermal expression of ATGL-1 is correlated with the late mobilization of neutral lipids in hypodermis (Figs 1E and 3B). Considering the changes in ATP levels of *atgl-1(xd314)* mutants and the efficient rescue of *atgl-1(xd314)* embryonic lethality by hypodermal expression of ATGL-1 (Fig 3A and H), it is possible that during ventral closure the energy demand is high in hypodermis to support the extensive cellular movement. The developmental changes of the mitochondrial network in the embryonic hypodermis may be an active response to the increased energy demands or a passive adaptation in response to the availability of glycogen and neutral lipids. Mitochondrial fragmentation promotes fatty acid oxidation (Ngo *et al*, 2023). The hypodermal mitochondria exhibit a gradual transition from tubular to short rod shaped during embryonic development. The tubular mitochondria may fit with glycolytic metabolism and the short rod-shaped mitochondria may favor lipolytic metabolism. The embryonic lethality of *atgl-1(xd314)* could also be mildly rescued by expression of ATGL-1 in neurons, which may be related to the involvement of neuroblasts in ventral cleft closure.

The rescue of *atgl-1(xd314)* mutants by different manipulations indicates that there are several ways to overcome the potential energy deficit. Parental vitamin B12 supplement rescues *atgl-1(xd314)* accompanied by the presence of more wild-type-looking tubular and rod-shaped mitochondria. This suggests that improving mitochondrial function is an efficient approach to mitigate embryogenesis failure caused by defective lipolysis. On the other hand, the alleviation of the embryonic lethality of *atgl-1(xd314)* by glucose or

fatty acid supplements to parental worms is likely through provision of sufficient energy substrate. The mitochondrial fragmentation of *atgl-1(xd314)* is not rescued by glucose or fatty acid supplements. Instead, parental glucose and oleic acid supplements promote glycogen storage in embryos to circumvent impaired lipid mobilization.

Embryogenesis failure associated with defective lipolysis can also be rescued by loss of function of *sinh-1* or *age-1*. The mitochondrial defects of *atgl-1(xd314)* mutants are not rescued upon loss of function of *sinh-1* or *age-1*, indicating that the rescue is not through mitochondrial improvement. In line with this, instead of increasing mitochondrial activity, decreased insulin–Akt signaling activity causes mitochondria to enter a quiescent state via the remodeling of the mitochondrial electron transport chain during *Drosophila* oogenesis (Sieber et al, 2016). The *sinh-1/age-1-akt* signaling pathway is the core of the insulin and mTOR2 pathways, which play essential roles in glucose metabolism and are conserved across species. Although the detailed mechanism remains unclear, the suppression of embryonic lethality of *atgl-1(xd314)* by reducing the *sinh-1/age-1-akt* pathway is likely mediated through glucose metabolism. The glycogen content in *atgl-1(xd314)* embryos is significantly reduced, while the glucose level is maintained at a relatively high level. It is possible that reduced activity of the *sinh-1/age-1-akt* pathway may help to maintain the sustainable consumption of glucose, allowing the *atgl-1(xd314)* embryos to safely pass ventral morphogenesis. However, not all genes encoding the mTORC2 subunits have similar effects on *atgl-1(xd314)*. *riect-1/Rictor* RNAi cannot rescue the embryonic lethality of *atgl-1(xd314)*. *sinh-1* and *riect-1* may regulate *C. elegans* development through different downstream targets of mTORC2. *riect-1/Rictor* regulates *C. elegans* lipid storage and growth through *sgk-1/SGK-1*, a downstream target of mTORC2, but not by AKT kinases (Jones et al, 2009).

Our findings are in accordance with the central role of the insulin–Akt pathway in adaptation to metabolic alterations, probably by coordinating glucose usage. Reduced insulin signaling has been linked to adaptations to harsh environments. Nematodes enter the dauer phase to slow their metabolism and help them adapt to harsh environments, such as starvation and heat. Reduced insulin signaling promotes dauer formation in *C. elegans* (Riddle et al, 1981). Interestingly, diminished insulin signaling also helps cavefish adapt to prolonged periods of nutrient starvation (Riddle et al, 2018). A recent report showed that reducing the insulin–AKT signaling pathway promotes reproduction and longevity of *Harpegnathos* ants when they undergo caste transition (Yan et al, 2022).

Although defective mitochondria are found in both *C. elegans* and mouse ATGL mutants (Haemmerle et al, 2011), the importance of neutral lipids and lipolysis during embryonic development may vary in different species. It has been postulated that the lipid level in embryos is positively correlated with the time to implant in the uterus (Sturmey et al, 2009). Embryos of ruminants, pigs and dogs have a high-fat content, which may support the slow implantation of the embryo into the uterus. Mouse and human embryos implant in the uterus relatively quickly and may not require high levels of lipids as endogenous energy reserves (Sturmey et al, 2009). In placental species, the embryo can continuously obtain energy from the mother through the placenta after implantation. At this time, the acquisition of energy substances by embryos no longer depends solely on their own material reserves. Therefore, lipolysis-defective mutants are not embryonic lethal in placental species. In oviparous

animals, such as *Drosophila*, zebrafish, and nematodes, the embryos wholly depend on maternally loaded nutrients, and therefore impaired lipolysis may cause severe embryonic lethality (Gronke et al, 2005; Dutta & Sinha, 2017).

Further in-depth understanding of metabolic plasticity during embryogenesis will help us to learn how embryos cope with extrinsic and intrinsic metabolic alterations to sustain normal embryogenesis. The finding that metabolic plasticity ensures the robustness of embryogenesis offers new strategies to overcome potential developmental failure.

## Materials and Methods

### Strains

Worms were maintained at 22°C on nematode growth medium (NGM) plates seeded with *E. coli* OP50 (Brenner, 1974), unless otherwise specified. The *C. elegans* strains used in this study are listed in Appendix Table S1.

### Ethyl methanesulfonate (EMS) mutagenesis and SNP mapping

Ten plates of *atgl-1(xd314)* nematodes were synchronized to the L4 stage for EMS mutagenesis. The EMS-treated nematodes were placed on NGM plates and incubated at 22°C for 4 h. A total of 200 nematodes (P0) at the late L4 stage were picked from the NGM plate and cultured three per plate for 3 days. Then, 200 nematodes (F1) were taken from the P0 plate and plated three per plate. After 7 days, the plates were examined for food consumption. Two nematodes were taken from the plate where the food had almost been consumed and cultivated individually. The plates with fast food consumption were retained. The procedure was repeated several times to obtain a stable fast food consumption strain. The hatching rate was measured for the strains with fast food consumption. If the hatching rate was significantly higher than that of *atgl-1(xd314)*, it was considered as a suppressor strain of *atgl-1(xd314)*. To map the chromosomal location of the suppressor mutation, we used the single nucleotide polymorphism mapping (SNP) method as previously described (Davis et al, 2005). Whole-genome sequencing was performed to further identify candidate genes combined with the results of genetic mapping.

### Molecular biology

For *xdKi24(atgl-1::gfp knock-in)*, the GFP is inserted at the C-terminal end. For *xdKi87(gfp::akt-1 knock-in)*, the GFP is inserted at the N-terminal end. For *xdEx3335(Pakt-1::GFP)*, a 3,251-bp *akt-1* promoter fragment was amplified from N2 genomic DNA and inserted into plasmid pPD95.75. The promoters of *ajm-1*, *rab-3*, *vha-6*, *Y37A1B.5*, *atgl-1*, and *sinh-1* were amplified from N2 genomic DNA. The coding regions of *atgl-1* and *sinh-1* were amplified from cDNA. The promoter and corresponding cDNA were cloned into  $\Delta$ pSM vectors using standard protocols and were verified by sequencing.

Total RNA was isolated using TRIzol reagent (Invitrogen). cDNA synthesis was performed using M-MLV reverse transcriptase (Invitrogen SuperScript III) with 1–3 mg of RNA. Real-time quantitative

PCR (qRT-PCR) was carried out on a 7500 Real-Time PCR machine from Applied Biosystems using SYBR Green Supermix (Transgen Biotech, Beijing, China). Results were calculated using Ct values and normalized to *act-1* mRNA level. The primer sequences for qRT-PCR are listed in Appendix Table S2.

### Staining and image analysis

To measure glycogen content *in vivo*, day 1 adult worms were stained with iodine vapor as previously described (Frazier 3rd & Roth, 2009). The worms were transferred to a fresh plate, which was then inverted and placed on top of a 100 g bottle of iodine (Aladdin) for 2 min. Images were captured using Nikon Eclipse 90i. For neutral lipid staining, embryos were collected and rinsed in M9. The eggshells were digested with 2 mg/ml chitinase (Sigma) for 10 min. Then, embryos were stained for 1 h with 2 µg/ml Bodipy (Invitrogen) and shaken gently in the dark for 1 h. For adults, day 1 adult worms were incubated in 500 µL M9 with 10 µg/ml Bodipy (Invitrogen) and shaken gently in the dark for 5 h. Then, worms were recovered after 15 min. Images were captured by confocal microscopy. Oil Red O staining was performed as previously described (O'Rourke et al, 2009). Images were captured using a Nikon Eclipse 90i. The staining intensities in the anterior intestinal region were quantified.

For ATP analysis, Perceval HR was excited using 488 and 405 nm lasers, corresponding to the ATP-bound and ADP-bound conformation, respectively. Emission was collected through a 405- to 550-nm band-pass filter. Images were captured by confocal microscopy. The hypodermal marker  $P_{Y37A1B.5}::mCherry$  was used for colabeling with lipid droplets (stained with Bodipy) and ATGL-1::GFP in embryos. The mean fluorescence density was calculated at the location of the hypodermal cells and in the rest of the embryo. The pictures for fluorescence quantitative analysis are all comma-stage embryos. Colocalization analysis was performed on confocal z-sections using ImageJ software.

For MitoTracker Red staining, day 1 adult worms were incubated in 500 µL M9 with 500 nmol/l MitoTracker Red CMXRos (Invitrogen) and shaken gently in the dark for 12 h. The eggs were then dissected out of the worms and imaged with a confocal microscope. For mitochondrial morphology analysis, according to the morphology of mitochondria, we divided mitochondria into four types: tubular, intermediate, rod-shaped, and spherical mitochondria. We counted the number of embryos of different genotypes with different mitochondrial morphologies under different treatment conditions using a fluorescence microscope.

We used AJM-1::GFP to label the cell membrane of hypodermal cells and performed 4D imaging using a spinning-disk confocal microscope as previously described (Ma et al, 2021). For tracking the embryonic development process, young adult worms were dissected and early embryos were released in M9. Embryos were transferred to a 2% agar pad, then the slides were blocked with dissolved wax and injected with egg salt. The Z-stack imaging range and spacing, as well as the time span and interval, were set, and imaging was performed overnight at 22°C using a fluorescence microscope.

For 3D reconstruction, we used *yqIs157(P<sub>Y37A1B.5</sub>::mito-GFP)*, which labels mitochondria in hypodermal cells, to observe the morphology of mitochondria in gastrulation-stage and comma-stage embryos. Images were captured using a confocal microscope. To reconstruct the mitochondria in embryos, the images were analyzed

using IMARIS 9 software. After aligning the Z-stacks, the mitochondria were traced and 3D-reconstructed in embryos. We set the color of the mitochondria as green and the rest of the embryo as blue.

To visualize organelle interactions, hypodermal lipid droplets and mitochondria were labeled by PLIN-1::mCherry and mito::GFP, respectively. Animals expressing the organelle-specific reporters were cultured on the indicated RNAi or control diets from birth to middle L4 stage. Then, the hypodermal segments localized in the anterior third of the body were imaged by spinning-disk confocal microscopy (Zeiss) at a 0.27-µm z-axis interval. The signals of the reporters were deconvoluted to gain clear borders of the organelles. To quantify the changes in the organelles and their interaction, the hypodermal lipid droplets and mitochondria were firstly reconstituted according to preprocessed signals using the surface function of Imaris 9.6.0 software. Then, the contact areas between the reconstituted organelles were computed by an Imaris plugin named Surface-Surface Contact Area. Lastly, the 3D views of the deconvoluted signals and reconstituted structures were output for display. The statistics of the reconstituted structures were calculated in Imaris and analyzed in GraphPad Prism 8.0 (GraphPad Software, Inc.).

### Biochemical analysis

The glycogen colorimetric assay kit II (K648-100, BioVision) was used to assess glycogen content in embryos as previously described (Gusarov et al, 2017). We collected 20-µl embryos and lysed them by sonication with 200 µl of lysis buffer. The samples were then centrifuged at 13,680 g at 4°C for 10 min to collect the supernatant. Next, we boiled the samples for 10 min, centrifuged them at 13,680 g for 10 min at 4°C, and collected the supernatant, then took 25 µl to measure the glycogen concentration. The total amount of glycogen was normalized to the total protein in the sample.

Invitrogen™ Amplex™ Red Glucose and a glucose oxidase assay kit (A22189) were used to assess glucose content and glucose oxidase activity in embryos, respectively. ATP determination kits (A22066) were used to measure ATP in embryos. The sample preparation method is the same as described for the glycogen colorimetric assay kit II above. The results were normalized to the total protein in the sample.

### Collection of early-stage and late-stage embryos

Firstly, the worms were synchronized by bleach. When the worms reached the young adult stage, the early-stage embryos were collected by bleach treatment. The late-stage embryos were collected from day 2 adults after 2 h of egg laying. Then, the embryos were snap-frozen in liquid nitrogen and stored at -80°C.

### mtDNA measurement

Mitochondrial DNA (*nduo-1*) copy number, normalized to nuclear DNA (*ges-1*), was assessed by qPCR using 50-ng total genomic DNA. Genomic DNA was extracted by a TIANamp Genomic DNA Kit.

### Hatching rate assay and starvation analysis

Eight L4-stage hermaphrodites were cultured one per plate on NGM plates. After incubating for about 2 days, the single worm was



removed. After 24 h, the number of unhatched eggs and the number of hatched eggs (i.e., the number of hatched worms) in the plate were counted. Hatching rate = number of hatched eggs / (number of hatched eggs + number of unhatched eggs). For starvation analysis, L4-stage nematodes were picked into bacteria-free NGM plates for the corresponding starvation time, and then Oil Red O staining was carried out.

### Dietary supplementation

For glucose feeding, glucose was mixed in the NGM plates to a final concentration of 2% as previously reported (Gusarov *et al.*, 2017). Synchronized L1-stage worms were maintained on the NGM plates with or without 2% glucose for hatching rate experiments, mitochondrial morphology assays, and glycogen assays. For fatty acid feeding, oleic acid (Sigma-Aldrich) was mixed in the NGM plates to a final concentration of 2 mmol. Synchronized L1-stage worms were maintained on the NGM plates with or without oleic acid for all assays.

### RNAi treatments

RNAi bacterial culture and RNAi plate preparation were carried out as previously described (Liu *et al.*, 2014). Empty L4440 vector was used as a negative control. Eight L4-stage hermaphrodites were placed on the corresponding RNAi plate, one worm per plate. The single worm was taken out after incubation for about 2 days, and the hatching rate was calculated after 24 h.

### Antibodies and western blotting

Antibodies against GFP (1:1,000, ab290) and  $\alpha$ -tubulin (1:1,000, ab18251) were purchased from Abcam. Antibody against Phospho-Threonine/Tyrosine (1:500, 9381) was purchased from Cell Signaling Technology. GFP-Trap resin to pull down AKT-1::GFP was purchased from Chromotek.

For protein sample preparation, synchronized L1 animals were cultured on NGM plates at 22°C for 3 days. Worms were harvested and washed with M9 3 times, then lysed in lysis buffer (50 mM Tris-HCl, pH 7.5, 150 mM NaCl, 10% glycerol, 1 mM PMSF, and 1% NP-40) with protease inhibitor cocktail (Roche) and phosphatase inhibitor cocktail (Roche). The lysate supernatant was collected after centrifugation at 12,000 g at 4°C for 10 min. For western blotting, the protein samples were run on SDS-PAGE gels and transferred to nitrocellulose membranes (1215458, GVS), then blocked with 5% nonfat milk. The signals were visualized with a High-sig ECL Western Blotting Substrate kit (Tanon). Western blot results were quantified by ImageJ software.

### Statistical analysis

All experiments in our study were repeated at least three times with similar results. For phenotype analysis, the worms were randomly selected from the plates to study. Additionally, we invited others in our laboratory to double-check the phenotypes without informing them of the genotypes or treatment conditions of the samples. Statistical analysis was performed by Prism v8 (GraphPad software). Data are presented as the mean  $\pm$  standard error of mean (SEM). Comparisons of two groups were performed using the unpaired two-tailed

Student's *t*-test. Comparisons between two or more groups were performed using one-way or two-way analysis of variance (ANOVA) with Tukey's correction for multiple comparisons. *P*-values are used to report whether there is a significant difference and are indicated with an asterisk (\*). \**P* < 0.05, \*\**P* < 0.01, \*\*\**P* < 0.001, \*\*\*\**P* < 0.0001.

## Data availability

This study includes no data deposited in external repositories.

**Expanded View** for this article is available [online](#).

### Acknowledgements

We thank Drs. Xiaochen Wang, Chonglin Yang, Mengqiu Dong, Suhong Xu, Ye Tian, and Pingsheng Liu for providing reagents and helpful discussions. This research was supported by grants 32230044, 32321004, and 91954207 from the National Natural Science Foundation of China.

### Author contributions

**Siyu Chen:** Conceptualization; validation; investigation; writing – original draft. **Xing Su:** Investigation. **Jinglin Zhu:** Investigation. **Long Xiao:** Investigation. **Yulin Cong:** Investigation. **Leilei Yang:** Formal analysis; investigation. **Zhuo Du:** Supervision; methodology. **Xun Huang:** Conceptualization; supervision; funding acquisition; writing – original draft; project administration; writing – review and editing.

### Disclosure and competing interests statement

The authors declare that they have no conflict of interest.

## References

- Arena R, Bisogno S, Gasior L, Rudnicka J, Bernhardt L, Haaf T, Zacchini F, Bochenek M, Fic K, Bik E *et al* (2021) Lipid droplets in mammalian eggs are utilized during embryonic diapause. *Proc Natl Acad Sci U S A* 118: e2018362118
- Benador IY, Veliova M, Mahdaviani K, Petcherski A, Wikstrom JD, Assali EA, Acin-Perez R, Shum M, Oliveira MF, Cinti S *et al* (2018) Mitochondria bound to lipid droplets have unique bioenergetics, composition, and dynamics that support lipid droplet expansion. *Cell Metab* 27: 869–885
- Brenner S (1974) The genetics of *Caenorhabditis elegans*. *Genetics* 77: 71–94
- Chen PH, Tjong WY, Yang HC, Liu HY, Stern A, Chiu DTY (2022) Glucose-6-phosphate dehydrogenase, redox homeostasis and embryogenesis. *Int J Mol Sci* 23: 2017
- Davis MW, Hammarlund M, Harrach T, Hullett P, Olsen S, Jorgensen EM (2005) Rapid single nucleotide polymorphism mapping in *C. elegans*. *BMC Genomics* 6: 118
- Dunning KR, Russell DL, Robker RL (2014) Lipids and oocyte developmental competence: the role of fatty acids and beta-oxidation. *Reproduction* 148: R15–R27
- Dutta A, Sinha DK (2017) Zebrafish lipid droplets regulate embryonic ATP homeostasis to power early development. *Open Biol* 7: 170063
- Frazier HN 3rd, Roth MB (2009) Adaptive sugar provisioning controls survival of *C. elegans* embryos in adverse environments. *Curr Biol* 19: 859–863
- Gardner DK, Leese HJ (1988) The role of glucose and pyruvate transport in regulating nutrient utilization by preimplantation mouse embryos. *Development* 104: 423–429

- Gardner DK, Pool TB, Lane M (2000) Embryo nutrition and energy metabolism and its relationship to embryo growth, differentiation, and viability. *Semin Reprod Med* 18: 205–218
- Ghosh S, Korte A, Serafini G, Yadav V, Rodenfels J (2022) Developmental energetics: Energy expenditure, budgets and metabolism during animal embryogenesis. *Semin Cell Dev Biol* 22: 00076-3
- Gottlieb S, Ruvkun G (1994) *daf-2*, *daf-16* and *daf-23*: genetically interacting genes controlling dauer formation in *Caenorhabditis elegans*. *Genetics* 137: 107–120
- Gronke S, Mildner A, Fellert S, Tennagels N, Petry S, Muller G, Jackle H, Kuhnlein RP (2005) Brummer lipase is an evolutionary conserved fat storage regulator in *Drosophila*. *Cell Metab* 1: 323–330
- Gusarov I, Pani B, Gautier L, Smolentseva O, Eremina S, Shamovsky I, Katkova-Zhukotskaya O, Mironov A, Nudler E (2017) Glycogen controls *Caenorhabditis elegans* lifespan and resistance to oxidative stress. *Nat Commun* 8: 15868
- Haemmerle G, Moustafa T, Woelkart G, Buttner S, Schmidt A, van de Weijer T, Hesselink M, Jaeger D, Kienesberger PC, Zierler K et al (2011) ATGL-mediated fat catabolism regulates cardiac mitochondrial function via PPAR-alpha and PGC-1. *Nat Med* 17: 1076–1085
- Hansen M, Hsu AL, Dillin A, Kenyon C (2005) New genes tied to endocrine, metabolic, and dietary regulation of lifespan from a *Caenorhabditis elegans* genomic RNAi screen. *PLoS Genet* 1: 119–128
- Ibayashi M, Aizawa R, Mitsui J, Tsukamoto S (2021) Homeostatic regulation of lipid droplet content in mammalian oocytes and embryos. *Reproduction* 162: R99–R109
- Jones KT, Greer ER, Pearce D, Ashrafi K (2009) Rictor/TORC2 regulates *Caenorhabditis elegans* fat storage, body size, and development through *sgk-1*. *PLoS Biol* 7: 604–615
- Kim J, Guan KL (2019) mTOR as a central hub of nutrient signalling and cell growth. *Nat Cell Biol* 21: 63–71
- Kimura KD, Tissenbaum HA, Liu YX, Ruvkun G (1997) *daf-2*, an insulin receptor-like gene that regulates longevity and diapause in *Caenorhabditis elegans*. *Science* 277: 942–946
- Kitano H (2004) Biological robustness. *Nat Rev Genet* 5: 826–837
- Lamming DW, Sabatini DM (2013) A central role for mTOR in lipid homeostasis. *Cell Metab* 18: 465–469
- Lass A, Zimmermann R, Haemmerle G, Riederer M, Schoiswohl G, Schweiger M, Kienesberger P, Strauss JG, Gorkiewicz G, Zechner R (2006) Adipose triglyceride lipase-mediated lipolysis of cellular fat stores is activated by CGI-58 and defective in Chanarin-Dorfman Syndrome. *Cell Metab* 3: 309–319
- Lee JH, Kong J, Jang JY, Han JS, Ji Y, Lee J, Kim JB (2014) Lipid droplet protein LID-1 mediates ATGL-1-dependent lipolysis during fasting in *Caenorhabditis elegans*. *Mol Cell Biol* 34: 4165–4176
- Lin K, Dorman JB, Rodan A, Kenyon C (1997) *daf-16*: an HNF-3/forkhead family member that can function to double the life-span of *Caenorhabditis elegans*. *Science* 278: 1319–1322
- Liu GY, Sabatini DM (2020) mTOR at the nexus of nutrition, growth, ageing and disease (vol 29, pg 145, 2020). *Nat Rev Mol Cell Biol* 21: 246
- Liu P, Gan W, Inuzuka H, Lazorchak AS, Gao D, Arojo O, Liu D, Wan L, Zhai B, Yu Y et al (2013) Sin1 phosphorylation impairs mTORC2 complex integrity and inhibits downstream Akt signalling to suppress tumorigenesis. *Nat Cell Biol* 15: 1340–1350
- Liu Z, Li X, Ge Q, Ding M, Huang X (2014) A lipid droplet-associated GFP reporter-based screen identifies new fat storage regulators in *C. elegans*. *J Genet Genomics* 41: 305–313
- Ma X, Zhao Z, Xiao L, Xu W, Kou Y, Zhang Y, Wu G, Wang Y, Du Z (2021) A 4D single-cell protein atlas of transcription factors delineates spatiotemporal patterning during embryogenesis. *Nat Methods* 18: 893–902
- Mau KHT, Karimlou D, Barneda D, Brochard V, Royer C, Leeke B, de Souza RA, Pailles M, Percharde M, Srinivas S et al (2022) Dynamic enlargement and mobilization of lipid droplets in pluripotent cells coordinate morphogenesis during mouse peri-implantation development. *Nat Commun* 13: 3861
- Morris JZ, Tissenbaum HA, Ruvkun G (1996) A phosphatidylinositol-3-OH kinase family member regulating longevity and diapause in *Caenorhabditis elegans*. *Nature* 382: 536–539
- Narbonne P, Roy R (2009) *Caenorhabditis elegans* dauers need LKB1/AMPK to ration lipid reserves and ensure long-term survival. *Nature* 457: 210–214
- Ngo J, Choi DW, Stanley IA, Stiles L, Molina AJA, Chen PH, Lako A, Sung ICH, Goswami R, Kim MY et al (2023) Mitochondrial morphology controls fatty acid utilization by changing CPT1 sensitivity to malonyl-CoA. *EMBO J* 42: e111901
- Ogg S, Ruvkun G (1998) The *C. elegans* PTEN homolog, DAF-18, acts in the insulin receptor-like metabolic signaling pathway. *Mol Cell* 2: 887–893
- Ogg S, Paradis S, Gottlieb S, Patterson GI, Lee L, Tissenbaum HA, Ruvkun G (1997) The Fork head transcription factor DAF-16 transduces insulin-like metabolic and longevity signals in *C. elegans*. *Nature* 389: 994–999
- O'Rourke EJ, Soukas AA, Carr CE, Ruvkun G (2009) *C. elegans* major fats are stored in vesicles distinct from lysosome-related organelles. *Cell Metab* 10: 430–435
- Paonessa M, Borini A, Coticchio G (2021) Genetic causes of preimplantation embryo developmental failure. *Mol Reprod Dev* 88: 338–348
- Revtovich AV, Lee R, Kirienko NV (2019) Interplay between mitochondria and diet mediates pathogen and stress resistance in *Caenorhabditis elegans*. *PLoS Genet* 15: e1008011
- Riddle DL, Swanson MM, Albert PS (1981) Interacting genes in nematode dauer larva formation. *Nature* 290: 668–671
- Riddle MR, Aspiras AC, Gaudenz K, Peuss R, Sung JY, Martineau B, Peavey M, Box AC, Tabin JA, McGaugh S et al (2018) Insulin resistance in cavefish as an adaptation to a nutrient-limited environment. *Nature* 555: 647–651
- Rubio C, Simon C (2021) Embryo genetics. *Genes (Basel)* 12: 118
- Sakai N, Ohno H, Tomioka M, Iino Y (2017) The intestinal TORC2 signaling pathway contributes to associative learning in *Caenorhabditis elegans*. *PLoS One* 12: e0177900
- Scott R 3rd, Zhang M, Seli E (2018) Metabolism of the oocyte and the preimplantation embryo: implications for assisted reproduction. *Curr Opin Obstet Gynecol* 30: 163–170
- Sieber MH, Thomsen MB, Spradling AC (2016) Electron transport chain remodeling by GSK3 during oogenesis connects nutrient state to reproduction. *Cell* 164: 420–432
- Sturmey RG, Reis A, Leese HJ, McEvoy TG (2009) Role of fatty acids in energy provision during oocyte maturation and early embryo development. *Reprod Domest Anim* 44: 50–58
- Tantama M, Martinez-Francois JR, Mongeon R, Yellen G (2013) Imaging energy status in live cells with a fluorescent biosensor of the intracellular ATP-to-ADP ratio. *Nat Commun* 4: 2550
- Titchenell PM, Lazar MA, Birnbaum MJ (2017) Unraveling the regulation of hepatic metabolism by insulin. *Trends Endocrinol Metab* 28: 497–505
- Wei W, Ruvkun G (2020) Lysosomal activity regulates *Caenorhabditis elegans* mitochondrial dynamics through vitamin B12 metabolism. *Proc Natl Acad Sci U S A* 117: 19970–19981
- Wu G, Bazer FW, Cudd TA, Meininger CJ, Spencer TE (2004) Maternal nutrition and fetal development. *J Nutr* 134: 2169–2172

- Xiao L, Fan D, Qi H, Cong Y, Du Z (2022) Defect-buffering cellular plasticity increases robustness of metazoan embryogenesis. *Cell Syst* 13: 615–630
- Xie M, Roy R (2015a) AMP-activated kinase regulates lipid droplet localization and stability of adipose triglyceride lipase in *C. elegans* dauer larvae. *PLoS One* 10: e0130480
- Xie M, Roy R (2015b) The causative gene in Chanarian Dorfman Syndrome regulates lipid droplet homeostasis in *C. elegans*. *PLoS Genet* 11: e1005284
- Yan H, Opachaloemphan C, Carmona-Aldana F, Mancini G, Mlejnek J, Descostes N, Sieriebriennikov B, Leibholz A, Zhou X, Ding L et al (2022) Insulin signaling in the long-lived reproductive caste of ants. *Science* 377: 1092–1099
- Yang Q, Inoki K, Ikenoue T, Guan KL (2006) Identification of Sin1 as an essential TORC2 component required for complex formation and kinase activity. *Genes Dev* 20: 2820–2832
- Yang G, Murashige DS, Humphrey SJ, James DE (2015) A positive feedback loop between Akt and mTORC2 via SIN1 phosphorylation. *Cell Rep* 12: 937–943
- Yang L, Liang J, Lam SM, Yavuz A, Shui G, Ding M, Huang X (2020) Neuronal lipolysis participates in PUFA-mediated neural function and neurodegeneration. *EMBO Rep* 21: e50214
- Yuan HX, Guan KL (2015) The SIN1-PH domain connects mTORC2 to PI3K. *Cancer Discov* 5: 1127–1129
- Zhou JX, Wang X, Wang M, Chang YW, Zhang FX, Ban ZN, Tang RF, Gan QW, Wu SH, Guo Y et al (2019) The lysine catabolite saccharopine impairs development by disrupting mitochondrial homeostasis. *J Cell Biol* 218: 580–597
- Zhu H, Kartiko S, Finnell RH (2009) Importance of gene-environment interactions in the etiology of selected birth defects. *Clin Genet* 75: 409–423
- Zhu J, Lam SM, Yang L, Liang J, Ding M, Shui G, Huang X (2022) Reduced phosphatidylcholine synthesis suppresses the embryonic lethality of seipin deficiency. *Life Metab* 1: 175–189
- Zhu J, Meng W, Lam SM, Shui G, Huang X (2023) Phosphatidylcholine deficiency increases ferroptosis susceptibility in the *Caenorhabditis elegans* germline. *J Genet Genomics* 50: 318–329
- Zimmermann R, Strauss JG, Haemmerle G, Schoiswohl G, Birner-Gruenberger R, Riederer M, Lass A, Neuberger G, Eisenhaber F, Hermetter A et al (2004) Fat mobilization in adipose tissue is promoted by adipose triglyceride lipase. *Science* 306: 1383–1386